2015

Computational Study of Gas Separation Using Membrane

Nawaf Yahya Alkhamis
Lehigh University

COMPUTATIONAL STUDY OF GAS SEPARATION USING MEMBRANE

By

Nawaf Alkhamis

Presented to the Graduate and Research Committee of Lehigh University

In Candidacy for the Degree of

Doctor of Philosophy

In

Mechanical Engineering

Lehigh University

August, 2015

Approved and recommended for acceptance as a dissertation in partial fulfillment of the requirements for the degree of Doctor of Philosophy

_____
Accepted Date

_____
Dr. Alparslan Oztekin
Committee Chair

_____
Dr. Edmund Webb
Committee Member

_____
Dr. Keith Moored
Committee Member

_____
Dr. Raymond Pearson
Committee Member

ACKNOWLEDGMENT

I would like to express my appreciation to *Dr. Oztekin* for his support and guidance in the PhD program and research. Also, I would like to thank *Dr. Moored, Dr. Webb, and Dr. Pearson* for their support and for serving in my PhD committee.

I would like to express my sincere appreciation to my parents *Yahya Silman Alkhamis* and *Huda Nasser Alkhamees* for their support and love. I would like to express my worm thank to my wife, *Nour Jamal Alkhamees*, for her support and love and for helping me to complete my PhD degree. Also I like to thank my son *Abdulrahman Alkhamis* and my daughter *Deem Alkhamis*

CONTENTS

LIST OF FIGURE

LIST OF TABLE

NOMENCLATURE

C	concentration [mol/m^3]	C_F	drag coefficient of porous media
D	diffusion coefficient [m^2/s]	Dp^*	normalized Permeabilityof porous layer
D_2	hollow fiber membrane	D_1	lumen diameter
K	permeability of porous media	J	molar flux [mol/m^2]
M	molecular weight [g/mol]	L	membrane length [m]
P	permeance [$\frac{\text{mol}}{\text{m}^2\text{s Pa}}$]	$\dot{p}$	permeability [$\frac{\text{mol}}{\text{m s Pa}}$]
S	spacing between spacers [m]	Re	Reynolds number [-]
Sh	Sherwood number [-]	Sc	Schmidt number [-]
Vw	suction rate [m/s]	U	average velocity [m/s]
d	orifice diameter [m]	Y	mass fraction [-]
k	turbulent kinetic energy [J/kg]	hm	mass transfer coefficient [m/s]
m	mass flux [kg/(s m^2)]	l	membrane thickness [m]
u	x-component of velocity [m/s]	p	pressure [Pa]
x	x coordinate [m]	v	r-component of velocity [m/s]
Δp	pressure difference [Pa]	r	r coordinate [m]
α	mass selectivity [-]		
γ	rate of strain tensor	$\beta^*,\beta 1,\beta$	turbulent model parameters [-]
ρ	density [kg/m^3]	υ	kinematic viscosity [m^2/s]
σ,λ	turbulent model parameters [-]	ω	specific dissipation rate [1/s]
φ	porosity	$\boldsymbol{u}$	velocity vector

Subscripts and Superscripts

a and b	species: CO_2 or CH_4	w	properties at the membrane
i and j	index notation	T	eddy properties
CH_4	properties of CH_4	CO_2	properties of CO_2
tot	total properties	$\bar{}$	average property

ABSTRACT

Computational fluid dynamics simulations are conducted for multicomponent fluid flows in a channel containing spacers. The channel is bounded by membrane boundaries. A new and unique model has been presented for the treatment of the membrane boundaries in the separation of CO_2 from CH_4 in a binary mixture. The equation governing the flux through the membrane is derived from the first principle. The membrane is modeled as a functional surface, where the mass fluxes of each species will be determined based on the local partial pressures, the permeability, and the selectivity of the membrane. The approach introduced here is essential simulating gas-gas separation. Baseline Reynolds Stress, k-ω BSL, and Large Eddy Simulation, LES, turbulence models are employed to study spatial and temporal characteristics of the flow for a wide range of the Reynolds number. This study focuses on the improving the membrane performance by enhancing the momentum mixing in the feed channel by placing flow restricting bodies. The membrane properties such as membrane permeance and selectivity are fixed. Both spiral wound membrane and the hollow fiber membrane systems are considered here for gas separation applications. For the spiral wound membrane, it is shown here that the spacers have a strong effect on the membrane performance. The process of separating CO_2 from CH_4 is improved by the presence of spacers in the spiral wound membrane module. It is demonstrated that spacers should be an integral part of the membrane system design in the application of gas-gas separation. For the hollow fiber membrane it is illustrated here the porous support layer has strong influence on the membrane performance. Enhanced momentum mixing has been utilized to mitigate the adverse effects of the porous support layer. Flow restricting devices such as orifice,

diffuser and helical grooves and fins are considered to achieve the promotion of momentum mixing. It has been shown here that the hollow fiber membrane performance can be improved by careful design of these devices in the feed channel. Further study of optimization is essential to achieve better performance in hollow fiber modules.

Chapter 1: INTRODUCTION

Natural gas consumption has increased significantly in recent years. The impurities found in raw natural gas, extracted from underground, such as water vapor, carbon dioxide or hydrogen sulfide should be minimized to protect pipelines from corrosion. Membranes are used to separate these undesired gasses, thereby purifying the natural gas. In order to minimize capital and operation costs of the purification process, the membrane performance needs to be enhanced.

In the past, gas-gas separation using a membrane had been studied extensively by several investigators. Such studies include: improving the permeability and the selectivity of the membrane [1-5]; operating the membrane at the optimum temperature and pressure [6-8]; or improving the separation modules [9-11].

In the present study, the focus is less on these aspects of separation and more on enhancing the membrane performance using momentum mixing in the feed mixture and mass transfer enhancement. It is well known that the convective mass transfer in the flowing systems increase when turbulent mixing increases. However, the energy losses due to friction also increase due to turbulent mixing. The different type of turbulators produces different magnitude of turbulent mixing. This leads to the different level of improvement in mass transfer and different magnitude of increase in the frictional losses. Each turbulator might have a range that could improve the mass transfer more than increasing the frictional losses. By fixing the membrane specifications such as permeability and selectivity, and mixture and flow conditions such as the inlet mole fraction and the outlet pressure, this study investigate the effect of the different turbulators on the mass transfer through the membrane and the frictional losses. The

binary mixture, CH_4 and CO_2, in a spiral wound membrane and hollow fiber membrane are considered in this work. There have been extensive studies which show that enhanced momentum mixing in an open channel improves membrane performance in water treatment. However, the effect of mixing on the membrane's performance in gas-gas separation has not been studied. A unique model is presented for the treatment of the membrane boundaries; with which CO_2 absorption and CH_4 losses through the membrane are calculated for both cases. The membrane flux model derived from the first principle is necessary to accurately represents gas separation and is valid for the desalination process in the limit the concentration of the one of the component tends to zero.

Several investigators study the effects of momentum mixing on the membrane performance without considering the mass transport. Karode and Kumar[12] and Saeed et al.[13] consider a steady 3D laminar flow model to study the effects of a cylindrical spacer on the pressure drop at low Reynolds number for desalination process. The laminar model can be utilized when the Reynolds number is below the critical value for the transition to the turbulence. The laminar flow model fails to capture the flow physics in the high Reynolds number. In a typical gas separation process the Reynolds number is above the value of the critical Reynolds number for the onset of turbulence. Fimbres-Weihs et al.[14] and Ranade and Kumar[15] employed a direct numerical simulation (DNS) of the Navier-Stokes equation to study the effects of a cylindrical spacer on the pressure drop and the drag coefficient for a wide range of Reynolds numbers reaching above 1000. They have reported that the critical Reynolds number for the onset of transition from steady to unsteady flow occurs at around 300. Schwinge et al.[16] have studied how the staggered and the inline cylindrical spacers affect the flow field using

direct numerical simulations. The DNS is the most accurate model to characterize the flow characteristics; however the DNS required high computational time. To study the momentum mixing effect extensively, turbulent models that can capture the flow characteristics reasonably well and requires less computational resources are needed. Ranade and Kumar[17] studied three dimensional flows using the k-ε turbulent model to study the effects of cylindrical spacers on the pressure drop for values of the Reynolds number above 350. The k-ε turbulent model cannot predict the vortex shading behind the spacers. Several studies also introduced a mass transport equation, but still treated the membrane as an impermeable wall. Al-Sharief et al. [18] and Shakaib et al. [19] considered three dimensional flows by using a laminar model to study the effects of cylindrical spacers on the mass transfer in a water desalination process. This study also considered the flow for values of the Reynolds number below the critical value of the Reynolds number for the onset of transition to turbulence. A mass transport equation was also introduced by Al-Sharief et al [18]. They assumed that the mass flux of salt is constant on the membrane. Such assumption can be valid in desalination processes, but not in gas-gas separation processes. Shakaib et al. [19] assumed that the concentration at the membrane surface is constant. Several investigators improved upon the idea of treating the membrane surface as a permeable wall. Pal et al. [20] studied the effect of cylindrical spacers on the membrane performance for applications in the food industry. The membrane flux was assumed to be constant and a constant concentration at the surface of the membrane was assumed on a two-dimensional laminar flow model. Subramani et al. [21] and Guillen and Hoek [22] assumed that the flux through the membrane was constant and that the mass flux of the solute was constant. Both of these

studies used a laminar model to simulate characteristics of two dimensional flows in a water treatment process. Subramani et al. [21] considered two parallel membranes without spacers. Guillen and Hoek [22] studied the effects of different shapes of spacers on the membrane performance. Not considered in these previously mentioned studies, real separation processes through the membrane. The mass flux through the membrane should be modeled as a function of the local concentration and the osmotic pressure. Lyster and Cohen [23] , Villaluenga and Cohen[24], and Fletchera and Wiley [25] considered the local and osmotic pressures in their models. They assumed the mass flux of the salt was linearly proportional to that of the water. These studies considered a flow between two parallel membranes without any spacers. With a similar membrane model as what was employed in these aforementioned References [23-25], Fimbres-Weihs and Wiley[26] used a laminar model to study the effects of spacer orientation on the membrane performance in three dimensional flows. Ahmad and Lau[27], Lau et al.[28], Ma and Song[29] and Ma et al [30] used DNS approach and solve the Navier-Stokes equation for flow between two membranes with spacers. Ahmed and Lau studied the effects of different shapes of spacer attached on the membrane and Lau et al[28] studied the effects of cylindrical spacers on membrane performance. Ma and Song[29] and Ma et al [30] studied the effects of varying placements of square spacer on the membrane performance. Recently, Anqi et al. [31] studied the effect of momentum mixing on the membrane performance in a desalination process by a reverse osmosis. They have shown that by placing spacers in the feed channel membrane performance is enhanced greatly. Different shape, spacing and arrangements of spacers were studied by Ali et al. [31] by employing the large eddy simulation (LES) and SST turbulent model. They conducted

simulations for a wide range of the Reynolds number in a spiral wound membrane module for an application of brackish water desalination.

Kundu et al. [32, 33] employed Hagen- Poiseuille approximation to calculate the pressure drop along the lumen side of a hollow fiber membrane. Hagen-Poiseuille approximation assumes that the wall is impermeable and the radial component of the velocity is zero at the wall; these assumptions cannot be valid in a hollow fiber membrane module because the wall has to be permeable and there should be non-zero suction rate along the surface of the membrane. There is a vast amount of research in the field of only mass transport through the membrane is considered [34-39]. These studies do not consider the flow; or they de-couple the flow in the feed channel from the mass flux through the membrane. The importance of this coupling, and why it cannot be ignored, will be discussed later in this study. Vinther et al. [40] studied the dextran filtration process through a single hollow fiber membrane. Their work ignored the effects of the porous medium. Beavers et al. [41] experimentally studied flows in channels bounded by porous media. In their studies the porous layer was surrounded by an impermeable wall. This study validated the slip boundary conditions at the fluid-porous interface. For a channel bounded by a porous medium, Karode [42] developed an analytical solution for the pressure drop of a laminar fully-developed flow. Karode assumed a constant flux permeated across the walls. A number of studies coupled the Navier-Stokes equations and Darcy's law to model the case of an empty channel bounded by a porous medium [43-45]. The fluid considered in these studies was not a mixture; thereby, theirs studies only apply to filtration problems. Marcos et al. [46] conducted numerical simulations for flow in a HFM for applications in ultrafiltration systems for

protein concentration. Marcos' model accounted for the flow resistance caused by polarization, blockage, and cake; but the model did not incorporate the effects of a porous layer.

The aforementioned studies were focused on water desalination with membranes. The concentration of the salt in saline water ($mole_{salt}/mole_{water}$) varies from 0.002 to 0.04. The salt flux on the membrane is negligible when compared with the water flux. For the mass transport through the membrane, the salt flux can be assumed to be linearly proportional to the water flux in desalination processes. However, neither assumption can be used in the gas-gas separation where the concentrations of both species are comparable. In a model for gas-gas separation, the flux of both species has to be considered in the momentum and mass transports through the membrane. In the present study, the model presented considers these effects. This makes the model presented unique in both its ability to accurately model gas-gas separation and in its adaptability to other membrane flow applications. There exists no previous model which could study these flows without making some of the aforementioned assumptions about the membrane.

Chapter 2: GOVERNING EQUATION

2.1 Spiral Wound Membrane

Steady two dimensional flows of CH_4 and CO_2 binary mixture in a channel bounded by two parallel membranes are studied here for the Reynolds number from 200 to 1000 using a k-ω baseline Reynolds stress turbulence model. Transient two dimensional simulations are also conducted using both large eddy simulations (LES) and a k-ω BSL turbulence model for Re = 800 to investigate the effect of vortex shedding on the mass transport through the membrane. The aspect ratio of the computational domain is L/h = 120, where L is the channel length and h is the gap between two parallel membranes. The Reynolds number based on the inlet condition is $Re = Uh/\upsilon$, where U is the average fluid speed and υ is the kinematic viscosity. The schematic of the computational domain is illustrated in Fig. 1.

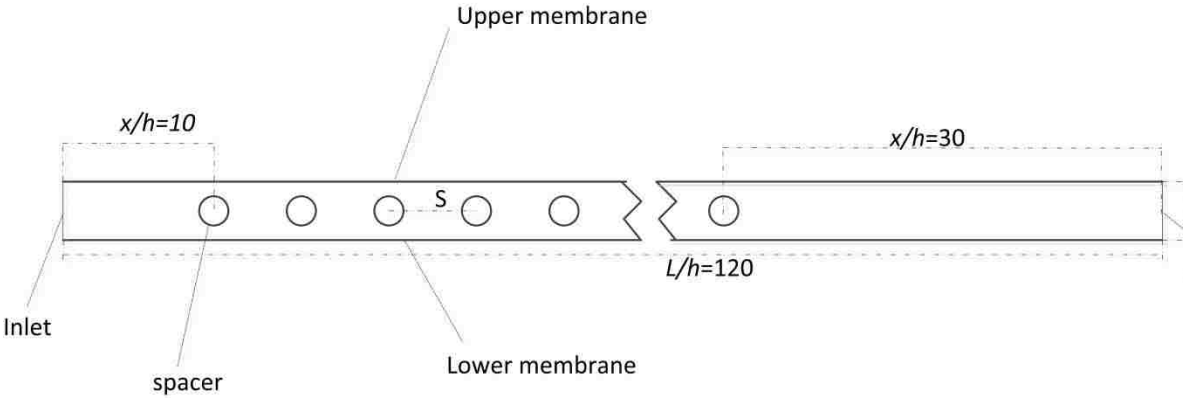

Figure 1: The schematic of the geometry for the spiral wound membrane system including spacers

The equations governing the laminar fluid motion inside the feed channel are Navier-Stokes equations of the form:

$$\frac{\partial u_j}{\partial x_j} = 0 \quad (1)$$

$$\frac{\partial u_i}{\partial t} + u_j \frac{\partial u_i}{\partial x_j} = -\frac{1}{\rho}\frac{\partial p}{\partial x_i} + \upsilon \frac{\partial^2 u_i}{\partial x_j \, \partial x_j} \quad (2)$$

Here j is the summation index and i can be either 1 or 2 for two dimensional flows. u_i is the fluid velocity vector, p is the pressure, x_i is the spatial coordinate, t is the time, υ is the kinematic viscosity, and $\rho = \rho_a + \rho_b$ is the density of the binary mixture where ρ_a and ρ_b are the density of species "*a*" and "*b*", respectively. $x \equiv x_1$ is the stream-wise direction, $y \equiv x_2$ is the span-wise direction; likewise, $u \equiv u_1$ is the stream-wise component of the velocity vector and $v \equiv u_2$ is the span-wise component of the velocity vector. The density of the mixture is assumed to be constant in equation (2). The mass transport equation for species "*a*" is of the form:

$$\frac{\partial CN_a}{\partial t} + u_j \frac{\partial CN_a}{\partial x_j} = D \frac{\partial^2 CN_a}{\partial x_j \partial x_j} \quad (3)$$

where D is the diffusion coefficient and $N_a = C_a/C$ is the mole fraction of species "*a*" in a binary mixture of CH_4 and CO_2. The total concentration in equation (3) is not treated as a constant.

Fimbres-Weihs et al.[14], Ranade and Kumar[15], and Schwinge et al[16] documented that the flow past arrays of spacers becomes transient and the Karman vortex shedding behind the spacers creates large and small eddies for values of *Re* above 300. It has been shown by Menter[47] that *k*-*ω* BSL turbulence model predicts turbulent flow near and outer wake region better for a large range Reynolds number. This method is improved version of the *k*-*ω* model and it captures separation better than both the original

k-ω and k-ε models. k-ω BSL turbulent model is employed to simulate flow past arrays of spacers for the range of *Re* considered here. The k-ω BSL turbulence model yields

$$\frac{\partial u_i}{\partial t} + u_j \frac{\partial u_i}{\partial x_j} = -\frac{1}{\rho}\frac{\partial p}{\partial x_i} + \frac{\partial}{\partial x_j}\left((\nu + \upsilon_T)\frac{\partial u_i}{\partial x_j}\right) \quad 4$$

where $u = u_1$, $v = u_2$, $x = x_1$ and $y = x_2$. $\upsilon_T = k/\omega$ is the eddy viscosity and is determined using

$$\frac{\partial k}{\partial t} + u_j \frac{\partial k}{\partial x_j} = \frac{\partial}{\partial x_j}\left((\nu + \sigma\upsilon_T)\frac{\partial k}{\partial x_j}\right) + \tau_{nj}\frac{\partial u_n}{\partial x_j} - \beta^* k\omega \quad 5$$

$$\frac{\partial \omega}{\partial t} + u_j \frac{\partial \omega}{\partial x_j} = \frac{\partial}{\partial x_j}\left((\nu + \sigma\upsilon_T)\frac{\partial \omega}{\partial x_j}\right) - \beta_1\omega^2 + \lambda\frac{\omega}{k}\tau_{nj}\frac{\partial u_n}{\partial x_j} + 2(1 - F_1)\frac{\sigma}{\omega}\frac{\partial k}{\partial x_j}\frac{\partial \omega}{\partial x_j} \quad 6$$

Here k is the turbulent kinetic energy, ω is the specific dissipation rate, and τ is the residual stress tensor. The constants are selected to be $\sigma = 0.5$, $\beta^* = 0.09$, $\beta_1 = 0.075$ and $\lambda = 0.556$ [47].In equations (5 and 6) both j and n are summation indices. The blending function F_1 is defined by [47]

$$F_1 = \tanh\left(\left[\max\left(\min\left(\frac{\sqrt{k}}{0.09\omega y^+}; .45\frac{\omega}{\Omega}\right); \frac{400\nu}{y^{+2}\omega}\right]\right)\right) \quad 7$$

where the Ω is absolute value of vorticity and y^+ is the distance to the nearest wall.

The species equation for the k-ω model is of the form:

$$\frac{\partial CN_a}{\partial t} + u_j \frac{\partial CN_a}{\partial x_j} = \frac{\partial}{\partial x_j}\left((D + \sigma D_T)\frac{\partial \rho C}{\partial x_j}\right) \quad 8$$

where D_T is the eddy diffusion coefficient. The turbulent Schmidt number,. Sc_T, is defined by

$$Sc_T = \frac{\nu_T}{D_T} \quad (9)$$

Sc_T and β are selected to be 0.85 and 0.09 in the present work. Na is the mole fraction of species "a", D is the diffusion coefficient and C is the concentration of the binary mixture.

In order to capture the effects of vortex shedding on the membrane performance, transient simulations are conducted using the transient k-ω BSL model and the LES turbulence model. The equations governing the LES model for incompressible flows are obtained by filtering the Navier-Stokes equation [48-52]

$$\frac{\partial u_i}{\partial x_i} = 0 \quad (10)$$

$$\frac{\partial u_i}{\partial t} + \frac{\partial u_i u_j}{\partial x_j} = -\frac{1}{\rho}\frac{\partial p}{\partial x_i} + \nu \frac{\partial^2 u_i}{\partial x_j \partial x_j} \quad (11)$$

where u_i and p are the filtered velocities and pressure fields calculated by equation 12. This represents interactions across both large and small scales.

$$\langle u_i(\boldsymbol{x},t)\rangle = \int_{-\infty}^{+\infty} u_i(\boldsymbol{x},t) g(\boldsymbol{x}',\boldsymbol{x}) \ , \quad \langle p(\boldsymbol{x},t)\rangle = \int_{-\infty}^{+\infty} p(\boldsymbol{x},t) g(\boldsymbol{x}',\boldsymbol{x}) \quad (12)$$

Where $g(\boldsymbol{x}',\boldsymbol{x})$ is filter function

At the inlet, the flow is fully developed and the concentration is constant, $N_{CH_4} = 0.7$. At the surface of the spacers, the no slip and no-penetration conditions are applied. The molar flux of each species is zero along the surface of the spacers. At the surface of the membrane, the no slip and the suction boundary conditions are imposed on the velocity field. The suction rate is calculated from local pressure and concentration. A detailed

description of the membrane model and the boundary conditions is given later in this chapter.

2.2 Hollow Fiber Membrane

The schematic of the flow geometry is illustrated in Figure 2. It consists of an open tubular channel surrounded by a porous layer which is bounded by a dense membrane. Uniformly spaced orifices are placed in an open channel. The diameter of the orifice is $d = 0.5\ D_1$ and the spacing between two consecutive orifice is $s = 20\ d$. The binary mixture of CH_4 and CO_2 is treated as an incompressible fluid with uniform physical properties. The flow is axisymmetric and isothermal. The diffusion coefficient is assumed to be independent of the concentration. The permeability of the porous layer is constant. The porous layer is considered to be saturated and the membrane selectivity and permeability is assumed to be constant.

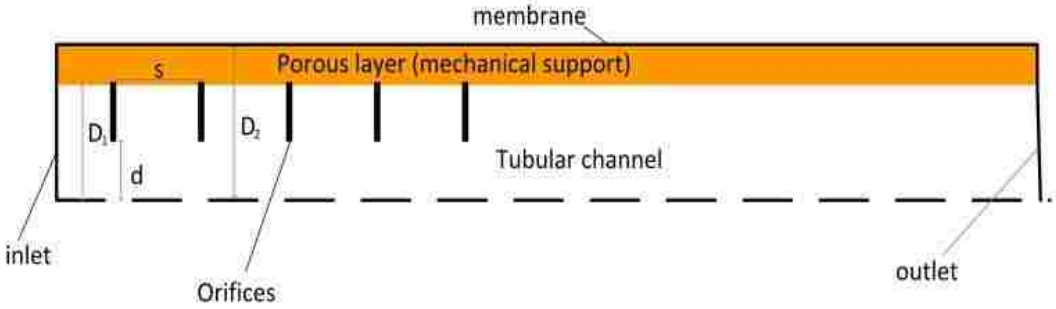

Figure 2: Schematic of the flow geometry and the membrane module

BSL Reynolds Stress turbulence model is employed to simulate flow inside the tubular channel. The equation governing the fluid motion is described in the previous section

In the porous layer, the mechanical support layer, the Brinkman-Forchheimer equation is employed[53]

$$\frac{\partial u_i}{\partial t} + u_j \frac{\partial u_i}{\partial x_j} = -\frac{1}{\rho}\frac{\partial p}{\partial x_i} + \frac{\partial}{\partial x_j}\left((\nu + \upsilon_T)\frac{\partial u_1}{\partial x_j}\right) - \phi\frac{v}{K}u_i - \frac{C_F}{K^{0.5}}|u_i|u_i \quad (13)$$

where the C_F is drag coefficient and K is permeability of the porous layer, ϕ is porosity. Here u = u_1, $v = u_2$, $x = x_1$ and $y = x_2$. $\upsilon_T = k/\omega$ is the eddy viscosity and is determined using the BSL Reynolds Stress turbulence model

$$\frac{\partial k}{\partial t} + u_j \frac{\partial k}{\partial x_j} = \frac{\partial}{\partial x_j}\left((\nu + \sigma\upsilon_T)\frac{\partial k}{\partial x_j}\right) + \tau_{nj}\frac{\partial u_n}{\partial x_j} - \beta^* k\omega \quad (14)$$

$$\frac{\partial \omega}{\partial t} + u_j \frac{\partial \omega}{\partial x_j} = \frac{\partial}{\partial x_j}\left((\nu + \sigma\upsilon_T)\frac{\partial \omega}{\partial x_j}\right) - \beta_1\omega^2 + \lambda\frac{\omega}{k}\tau_{nj}\frac{\partial u_n}{\partial x_j} + 2(1 - F_1)\frac{\sigma}{\omega}\frac{\partial k}{\partial x_j}\frac{\partial w}{\partial x_j} \quad (15)$$

Here k is the turbulent kinetic energy, ω is the specific dissipation rate, and τ is the residual stress tensor. The constants are selected to be σ = 0.5, β^* = 0.09, β_1 = 0.075 and λ = 0.556 [47]. The detailed description of the blending function, F_1, is described in the section 2.1. In equation (14 and 15) both j and n are summation indices.

The species equation for the BSL Reynolds stress model is described in the previous section.

The dimensionless parameters governing the velocity and the concentration field are the Reynolds number, *Re*, the Schmidt number, *Sc* and the Darcy number, *Dp**

$$Re = \frac{U D_2}{v},\ Sc = \frac{v}{D},\ Dp^* = \frac{2K}{D_2 - D_1} \quad (16)$$

Here U is the average velocity at the inlet. There are several aspect ratios that influence the flow characteristics in the feed channel and also affect the membrane performance: ratio of orifice spacing to orifice diameter, *S/d,* ratio of orifice diameter to open tube

diameter, d/D_1, and the ratio of open tube diameter to composite tube diameter, D_1/D_2. The composite tube consists of the open tubular channel and the porous support layer. Three different geometries considered in the present study: composite tube without orifices, composite tubes containing orifices with S/d of 10 and 20. D_1/D_2 is fixed in all three geometries as 0.67 and both composite tubes with orifices have the same ratio of $d/D_1 = 0.5$

At the inlet, the fully developed stream-wise component of the velocity profile that is documented in Ref [54] is applied. Simulations are conducted in a long hollow fiber membrane module without orifices. The radial component of the velocity and the concentration profile are calculated near the outlet. These profiles are employed as inlet profiles in membrane modules that include orifices. Figure 2 depicts profiles of the stream-wise component of the velocity, the radial component of the velocity and the CH_4 mass fraction imposed at the inlet in two composite membrane modules containing orifices for Re = 250 and Dp^* = 0.37. These inlet profiles have to be calculated for each value of the Reynolds number and Dp^*. At the outlet, the constant pressure condition is imposed on the velocity field and the zero gradient condition is imposed on the concentration field.

At the interface between the empty tube and the porous layer the velocity, the concentration, the static pressure, the shear and normal stresses, and the gradient concentration are continuous. The boundary condition imposed on the velocity field is different than that is applied by Beavers and Joseph [55]. Beavers and Joseph introduced a slip velocity at the interface and they assumed that the slip velocity is proportional to the shear rate at the permeable boundary. Such an approach is only necessary when

simplified Darcy's law is applied to model the pressure and the velocity field in the porous layer. Boundary conditions imposed on the velocity and concentration field are described in detail below.

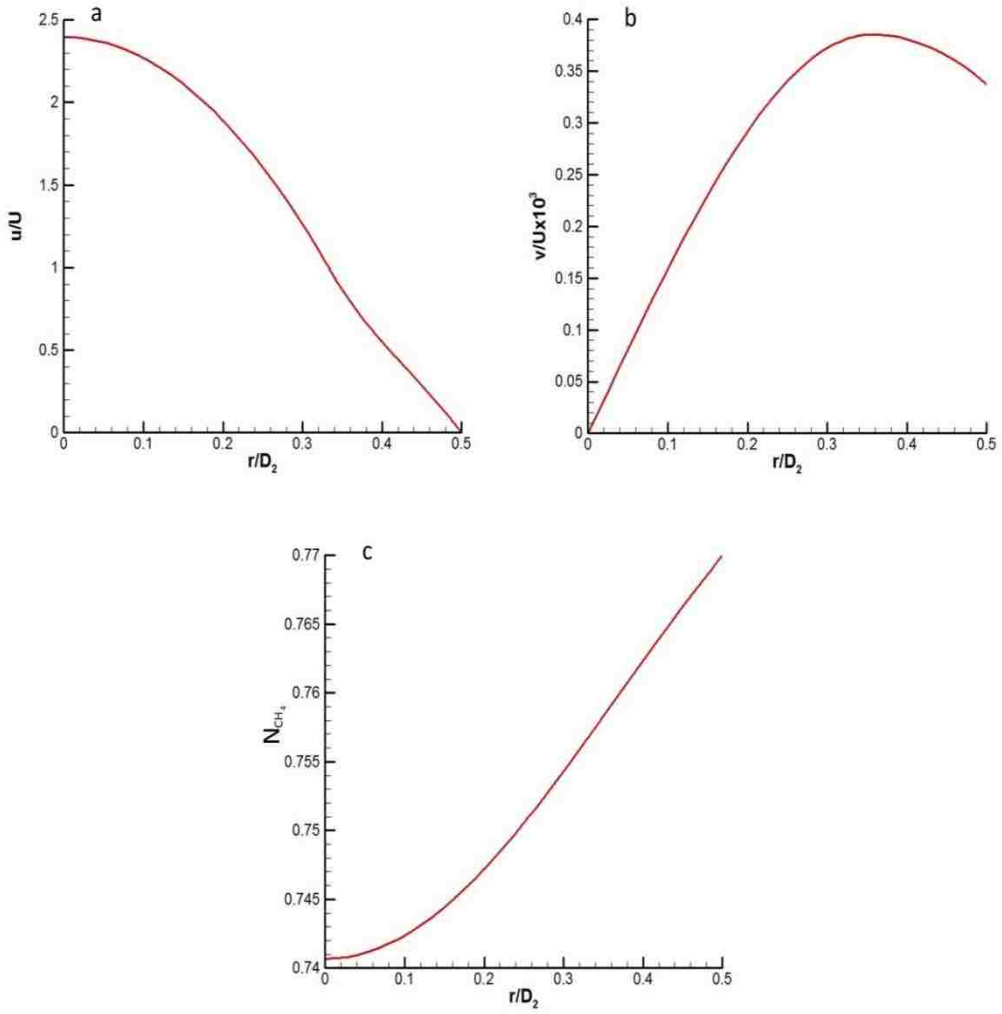

Figure 3: (a) The stream-wise component of the velocity, b) the radial component of the velocity, and c) the mole fraction profile at the inlet for *Re* = 250 and *Dp = 0.37**

2.3 Membrane Modeling and Boundary Condition

The molar flux through a membrane for a species "*a*" is given by

$$J_a = \frac{\overline{P_a}}{l}\left(p_a^{(1)} - p_a^{(2)}\right) = \frac{\overline{P_a}}{l}\Delta p_a \quad (17)$$

where J_a is the molar flux of species "a" per unit area extracted from the feed flow, l is the thickness of the membrane, $\overline{P_a}$ is the molar permeability of species "a", $\Delta p_a = \left(p_a^{(1)} - p_a^{(2)}\right)$ is the partial pressure difference of species "a" across the membrane. The molar flux (J) per unit area through the membrane can be determined as

$$J = J_a + J_b = \frac{\overline{P_a}}{l}\Delta p_a + \frac{\overline{P_b}}{l}\Delta p_b \quad (18)$$

Equation (18) can be rewritten in terms of molar selectivity, $\alpha = \overline{P_a}/\overline{P_b}$, as

$$J = \frac{\overline{P_b}}{l}[\alpha\Delta p_{tot} + (1-\alpha)\Delta p_b] \quad (19)$$

Here $\Delta p_{tot} = \Delta p_a + \Delta p_b$ is the total pressure difference across the membrane. With the definition of the permeance of species of "b" $P_b = \overline{P_b}/l$, the mass selectivity $\alpha = P_a/P_b$, and the relation between the partial pressure and the total pressure $\Delta p_a = N_a \Delta p_{tot}$ equation (18) yields

$$J = P_b\Delta p_{tot}[\alpha + (1-\alpha)Y_b] \quad (20)$$

The suction rate through the membrane can then be determined as

$$V_w = \frac{J}{C} = \frac{P_b\Delta p_{tot}}{C}[\alpha + (1-\alpha)N_b] \quad (21)$$

Here the suction rate, V_w, depends on the selectivity of the membrane, the permeability of the membrane, the pressure drop across the membrane, and the mole fractions of the species in the mixture, as depicted in equation (21).

The boundary conditions imposed on the velocity field at the surface of the membrane are: no-slip, $u = 0$, and the suction, $v = V_w$. No-slip and no-penetration at the surface of orifices are imposed.

The boundary conditions imposed on the mole fraction along the membrane is determined from the conservation of mass applied on the surface

$$J_a = -D\frac{\partial C_a}{\partial y} = -D\frac{\partial}{\partial y}(CN_a) \qquad 22$$

where Ca is the concentration of species "a". Accounting for the concentration variation and using equation (17) the boundary condition for the mole fraction of species "a" along the surface of membrane is derived as

$$\frac{\partial N_a}{\partial y} = \frac{\partial}{\partial y}\left(\frac{C_a}{C_a+C_b}\right) = \frac{1}{C^2}\left((C_a+C_b)\frac{\partial C_a}{\partial y} - C_a\frac{\partial}{\partial y}(C_a+C_b)\right) = \frac{1}{C^2}\left(C_b\frac{\partial C_a}{\partial y} - C_a\frac{\partial C_b}{\partial y}\right) \qquad 23$$

As shown in equation (23) the variation in total density is accounted for. Using equations (22) and (23) the boundary condition for the mass fraction of species "a" along the surface of the lower and the upper membrane is

$$D\frac{\partial N_a}{\partial y} = \frac{1}{C^2}\left(C_b D\frac{\partial C_a}{\partial y} - C_a D\frac{\partial C_b}{\partial y}\right) = \frac{1}{C^2}(-C_b J_a + C_a J_b) \qquad 24$$

Using the definition of mole fraction equation (24) yields

$$D\frac{\partial N_a}{\partial y} = \frac{1}{C}\left(-\frac{C_b}{C}J_a + \frac{C_a}{C}J_b\right) = \frac{1}{C}(-N_b J_a + N_a J_b) \qquad 25$$

Using the molar flux through the membrane given in equation (25)

$$J_a = P_a\Delta p_a \quad \text{and} \quad J_b = P_b\Delta p_b, \qquad 26$$

Equation (25) yields

$$D\frac{\partial N_a}{\partial y} = \frac{1}{C}(-N_b P_a \Delta p_a + N_a P_b \Delta p_b) \quad (27)$$

Using the definition of partial pressure and selectivity ($\alpha = P_a/P_b$) the boundary condition for the molar fraction at the surface of the membrane becomes

$$D\frac{\partial N_a}{\partial y} = \frac{1}{C}(N_b P_a \Delta p_a - N_a P_b \Delta p_b) = \frac{\Delta p_{tot} P_b}{C}(1-\alpha) N_a N_b \quad (28)$$

The separation model in this work is validated by comparing the predicted results against benchmark results. The membrane is considered to be a permeable wall and the flow is considered to be laminar in the channel without any spacers. At high Reynolds numbers, the flow is expected to behave similar to that of flow near an impermeable wall; this is because the suction rate is very small compared with main stream. The local value of the Sherwood number (*Sh*) is calculated and compared against the Sherwood number for a fully developed flow, as shown in Figure 4. The result predicted here for the developing flow tends to the fully developed value of *Sh* asymptotically with normalized downstream position. This proves that the membrane flux model is consistent with the benchmark value of the Sherwood number for laminar flows.

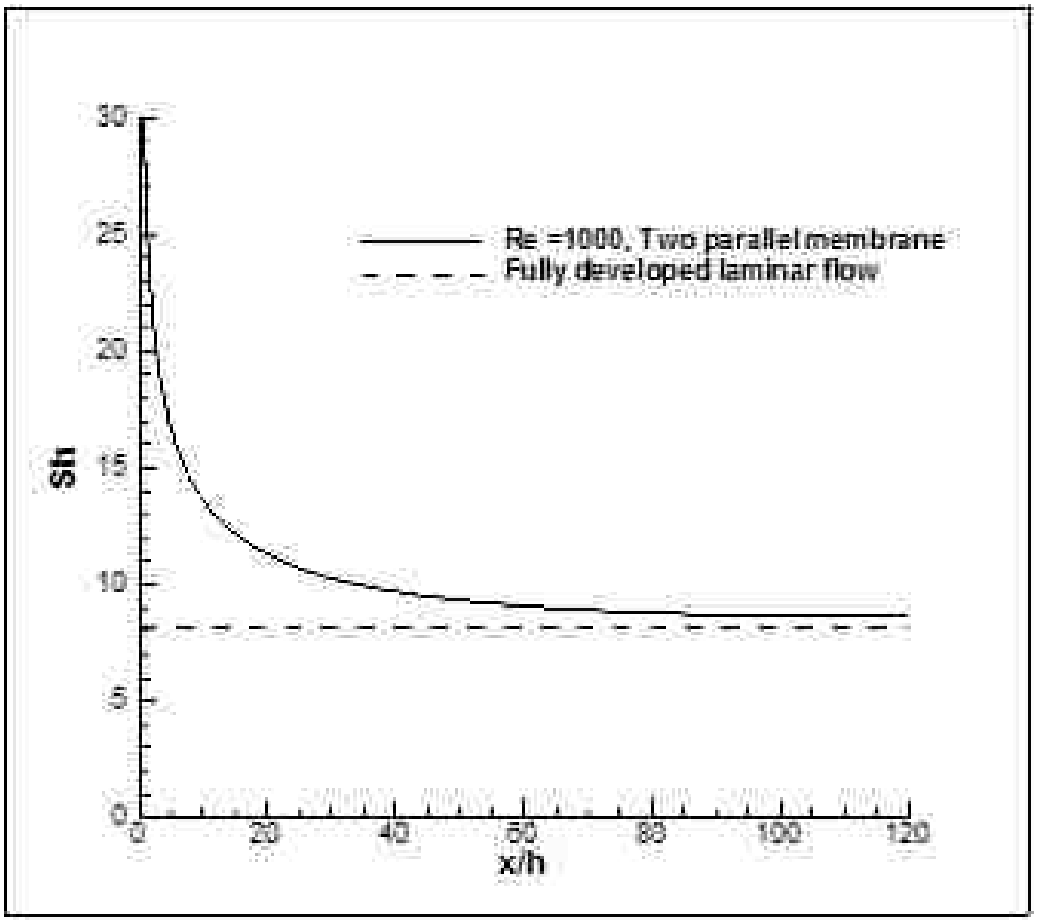

Figure 4: Local value of Sherwood number as a function of *x/h* for *Re* = 1000. Solid line denotes the results of the present numerical simulation while dashed line denotes the *Sh* for the fully-developed laminar flow

In the field of membrane science, the mass flux across the membrane is modeled by the classical equation:

$$-D\frac{\partial C_a}{\partial y} = RV_w C_a \qquad 29$$

Here R is the rejection rate of species "a". It can be seen that this new model, equation (28), and the common flux model, equation (29), are equivalent in the case where the rejection rate is

$$R = \frac{\alpha}{\alpha + (1-\alpha)N_b} \qquad 30$$

For desalination process, the permeation rate depends on the chemical potential differences and the rejection at the membrane depends on the reflection coefficient, the permeability and the flux, not on the concentration. Since the concentration of salt is very small, in the limit $N_b \rightarrow 0$ R approaches to 1. This is consistent with the equation (29) for the intrinsic rejection and majority of the investigations documented in the literature uses the instrinsic rejection as a constant near unity. For gas separation such limit is not valid since concentration of both species is comparable. The intrinsic rejection could vary significantly along the membrane. Figure 3 depicts the results of a sample simulation at a representative value of parameters, Re = 400, Dp^*=3.7, S/d = 20, P_{CO2} = 2.2x10^{-5} $\frac{\text{mol}}{\text{m}^2\text{s Pa}}$ and $\alpha = P_{CH4}/P_{CO2}$ = 0.0086, with and without orifices. Schmidt number is selected as 1.5 and a total pressure difference across the membrane is chosen as Δp_{tot} = 1 MPa. It clearly shows that the intrinsic rejection varies significantly along the membrane, as shown in Figure 3. This variation in the intrinsic rejection is realized in a short length of the membrane system considered here. In an actual membrane module, the intrinsic rejection will increase much more as the binary mixture becomes richer in CH_4. In fact, the intrinsic rejection can vary from nearly zero to nearly unity in the same purification process. It is also noted that the intrinsic rejection is lower when orifices are present, as shown in Figure 3. This is due to the fact that orifices promotes mixing and leads to more uniform concentration distribution across the cross-section of membrane module.

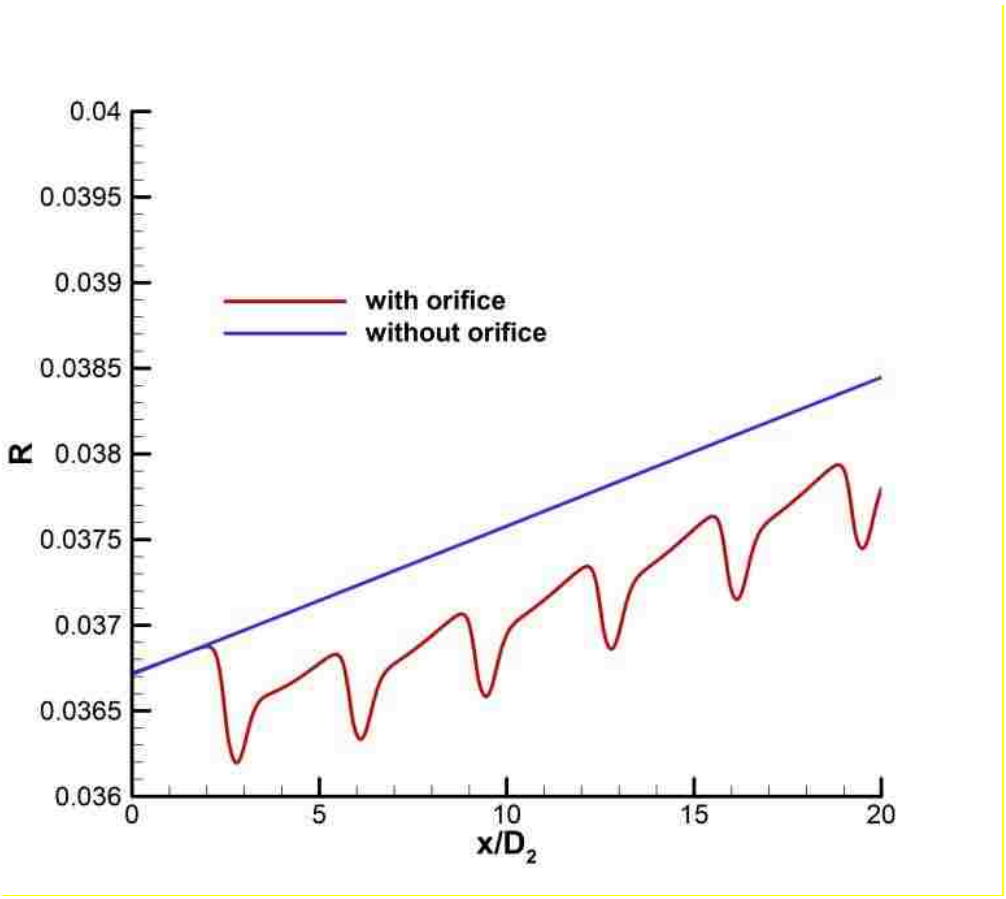

Figure 5:The profile of intrinsic rejection along the membrane at *Re* =400, *Dp=3.37, *S*/*d*=20 with and without orifices**

The mass transfer coefficient, the corresponding local Sherwood number, and the friction factor are determined from

$$h_m(x) = \frac{D\frac{\partial N_a}{\partial y}}{(N_m - N_w)}, \; Sh = \frac{h_m H}{D} \text{ and } f = \frac{2}{\rho U^2}\tau_w \qquad 31$$

where h_m is the mass transfer coefficient at x, N_m is the bulk mole fraction of the species "a", N_w is the mole fraction on the membrane of species "a", Sh is the local Sherwood number, f is the local friction factor and τ_w is the wall shear stress.

2.4 Numerical Method

Equations governing gas separation is strongly non-linear and is not possible to be solved analytically. Numerical methods are only alternative to obtain solutions to these coupled non-linear equations. The numerical methods such as finite difference, finite element and finite volume typically convert partial differential equations into discrete algebraic equations. The finite difference is the easiest technique to be implemented among the other numerical approach; however the finite difference method cannot be applied in the complicated geometry. The finite element method has more accurate prediction over the domain than the finite volume; but the finite volume method is commonly used in computational fluid dynamics simulations since the finite volume method satisfies the conversation laws automatically.

Commercial finite volume software, CFX 14.5, is employed to solve the continuity, the momentum and the mass transport equation. CEL expression language that is built in CFX is used to model the membrane. The permeance of CO_2 is P_{CO2} = $9.8\text{x}10^{-6}$ $\frac{g}{m^2 s\, pa}$ and the membrane mass selectivity is $\alpha = P_{CH4}/P_{CO2} = 0.0086$. The total density of the mixture is treated as constant in the momentum and continuity equations. The Schmidth number $Sc = \upsilon/D = 1.5$.

In order to test the spectral convergence for hollow fiber membrane, simulations for steady flow are conducted for $Re = 400$, $Dp^* = .037$ and $S/d = 10$ using $4.8\text{x}10^5$, $1\text{x}10^6$, and $1.5\text{x}10^6$ cells. The discharge coefficient is calculated as 0.717 for mesh $4.8\text{x}10^5$, 0.71 for mesh $1\text{x}10^6$ and, 0.708 for mesh $1.5\text{x}10^6$; ensuring the spatial convergence is attained with the mesh of $4.8\text{x}10^5$ cells for steady simulation. The discharge coefficient of each orifice is calculated from the pressure drop, Δp, across the orifice, by using the relation

$$C_d = \dot{m}/\left(A\sqrt{2\rho\Delta p}\right) \quad (32)$$

where A is the cross-sectional area of the orifice and $\dot{m}$ is the mass flow rate in the feed channel. Spatial convergence test is also conducted to calculate the Sherwood number along the membrane surface using $4.8\text{x}10^5$, $1\text{x}10^6$, and $1.5\text{x}10^6$ cells. Figure 4 shows the profiles of the Sherwood number predicted for *Re* = 400, *Dp**=0.037, and *S*/*d* = 10 using three different meshes. The profiles are nearly identical, that again ensures that the spatial convergence is achieved with the mesh of $4.8\text{x}10^5$ cells.

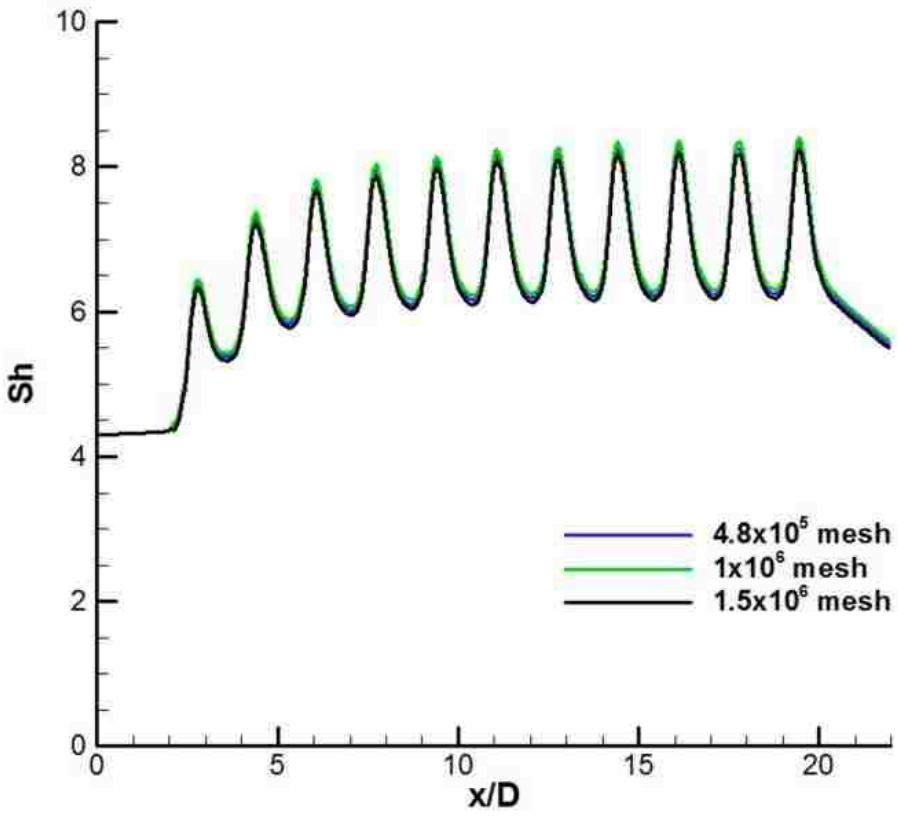

Figure 6: Profiles of the Sherwood number along the membrane surface for *Re* = 400, *Dp = 0.37 and *S/d* = 10 for three different meshes.**

For spiral wound membrane, steady flow simulations for *Re* = 1000 and *S/d* = 5 are conducted using $1.2x10^6$, $1.8x10^6$, and $2.1x10^6$ cells. Figure 7 shows the steady velocity profile at *x/h* = 6.25 in the middle between two spacer for inline cylinder arrangement with *S/d* = 5 at *Re* = 1000. The velocity profiles, predicted using three different mesh sizes ($1.2x10^6$, $1.8x10^6$ and $2.1x10^6$), are nearly identical and the drag coefficient was 1.405 for mesh $1.2x10^6$, 1.396 for mesh $1.8x10^6$ and, 1.384 for mesh $2.1x10^6$ The difference in the drag coefficient is less than 1.5%; that ensures the spectral convergence is attained with the mesh size of $1.2x10^6$ cells for both steady and transient

simulations. The results presented in the present study are obtained using $1.2x10^6$ cells for both steady and transient simulations. In order to obtain temporal convergence a time step of $8.0x10^{-6}$ for the LES and $2.5x10^{-5}$ for the transient BSL Reynolds Stress model is used. These time steps are small enough to capture the periodic nature of the Karman vortex street. The iteration stop when the residual in all flow properties reach below 1 x 10^{-6}.

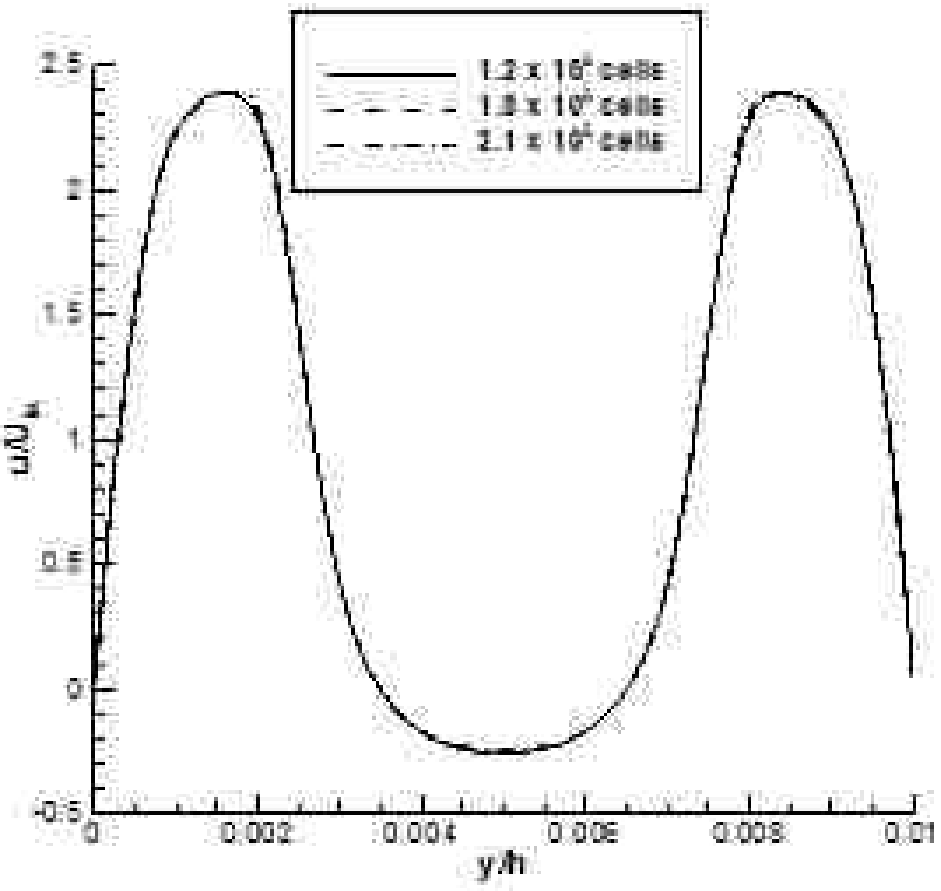

Figure 7: Velocity profile obtained using different meshes

Chapter3: SPIRAL WOUND MEMBRANE

3.1 Problem Description:

The geometry of the spiral wound membrane considered in the present study is a channel containing spacers, which is bounded by two parallel membranes. Two different arrangements of spacers are considered: the inline and the staggered arrangements. In inline arrangements, spacers are positioned directly behind one another and their axes are in the same *y* location. In the staggered arrangements, spacers are not aligned; their axes alternate between two different *y* locations. Circular and triangular cross-sectioned spacers are used in the simulations for both inline and staggered cases. The spacing between the cylinders is selected to be S/d = 10 and 5. For the staggered arrangement, the offset of the center of the cylinders is selected as St/d =1. Figure 8 depicts the mesh structure near the first cylinder in the channel. It is noted that the mesh spacing is finer inside the boundary layer. The same structure of mesh is used through the computational domain. The results presented in this chapter were published in References [56-59].

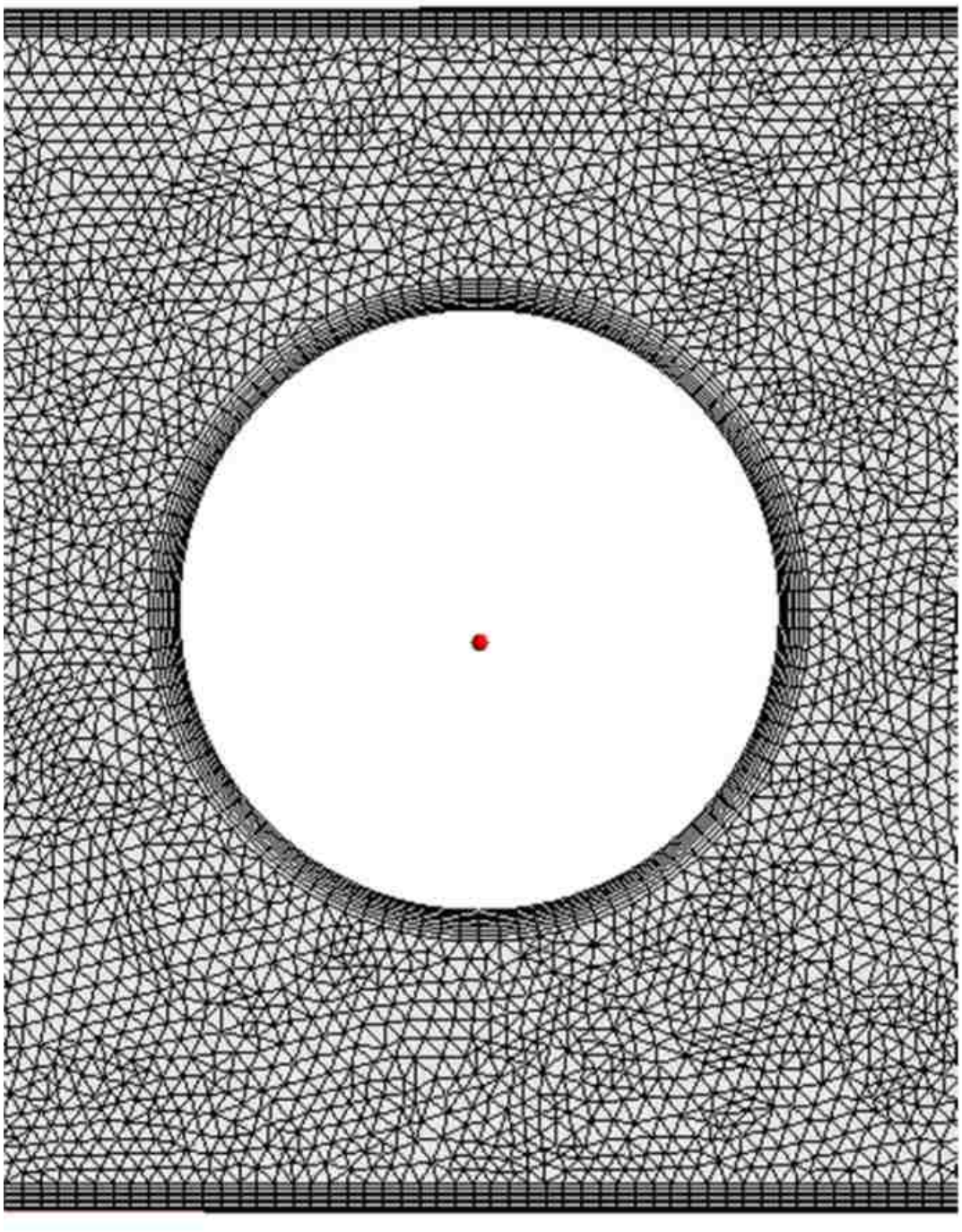

Figure 8: Meshing near a spacer in the feed channel

3.2 Method validation:

In order to validate the k-ω BSL model employed here simulations are conducted for flow past a rectangular cross-sectioned cylinder for $250 \leq Re \leq 1500$. The predicted values of average drag coefficient agree well with those measured by Davis et.al[60], as listed in Table 1. This illustrates that the k-ω BSL turbulence model is a good choice to simulate the flow in the geometry considered here for the range of Re studied.

Re	C_d experiments [60]	C_d k-ω BSL - Present	% Difference in C_d	DNS prediction [60]
250	1.95	1.93	% 1.2	1.64
500	2.16	2.06	% 4.6	
1000	2.37	2.10	% 7.1	1.88
1500	2.22	2.48	% 10.4	

Table 1: Comparison between the predicted and experimental results for the average value of the drag coefficient in flow past a rectangular cross-sectioned cylinder

3.3 Results and discussion

Figure 9 shows the steady state velocity vector and the contours of concentration of CH_4 around first two spacers in the channel for $Re = 500$ and $S/d = 10$. The velocity and the concentration fields are shown for inline and staggered arrangements of cylindrical spacers and the inline arrangement of triangle spacers. The steady-state flow structure illustrated in these images is a time averaged representation of what is, in reality, a periodic flow. The real flow structure is the classic case of a flow around a blunt

body, in which vortices form on alternating sides behind the body and shed periodically. This flow structure behind the body is called the Karman vortex street. There are notable differences in the flow structures between these images. Large and small eddies are present in the wake of each spacer and the middle region toward the membrane. The momentum mixing, caused by the Karman vortex street, results in more uniform distribution of concentration and the enhancement in the mass transfer through the membranes. The vortex shedding will also cause an increase in the pressure drop across the system; this must be taken into consideration if such a design is to be implemented in a real system.

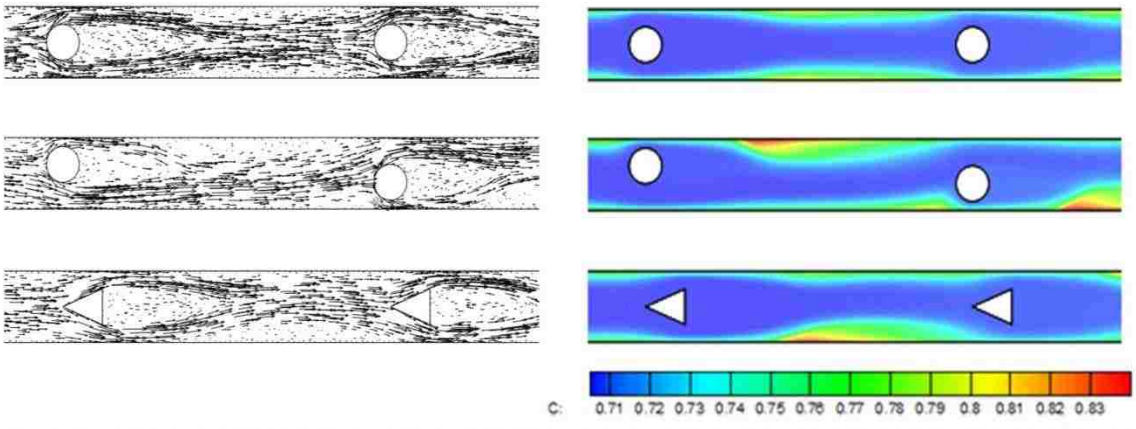

Figure 9: The velocity vector and the contours of concentration for *Re* = 500 and *S/d* = 10. Images on the left denote the velocity vector field and images on the right denote the contours of concentration. Images at the top and in the middle denote the inline and staggered geometries of circular spacers and the images at the bottom denote the inline geometry of triangular spacers

Figure 10 shows the suction rate along the membrane for *Re* = 200 and 1000 with *S/d* = 10. Suction rates in a feed channel containing inline and staggered arrangements of circular spacers and the inline arrangement of the triangular spacers are plotted in Figure 10. What is also shown in Figure 10 is the suction rate along the membrane for flows without the spacers for comparison purposes. The suction rate along the membrane

increases as *Re* is increased. The spacer's influence on the mass flux through the membrane is more pronounced for high Reynolds number flows, as shown in Figure 10. The effect of the spacers on the membrane performance is not as strong at low *Re* flows for all geometries considered here. The suction rate fluctuates along the membrane. It can be inferred from the data, that a local maximum forms near the spacer and a local minimum forms near the middle point between the spacers.

a)

b)

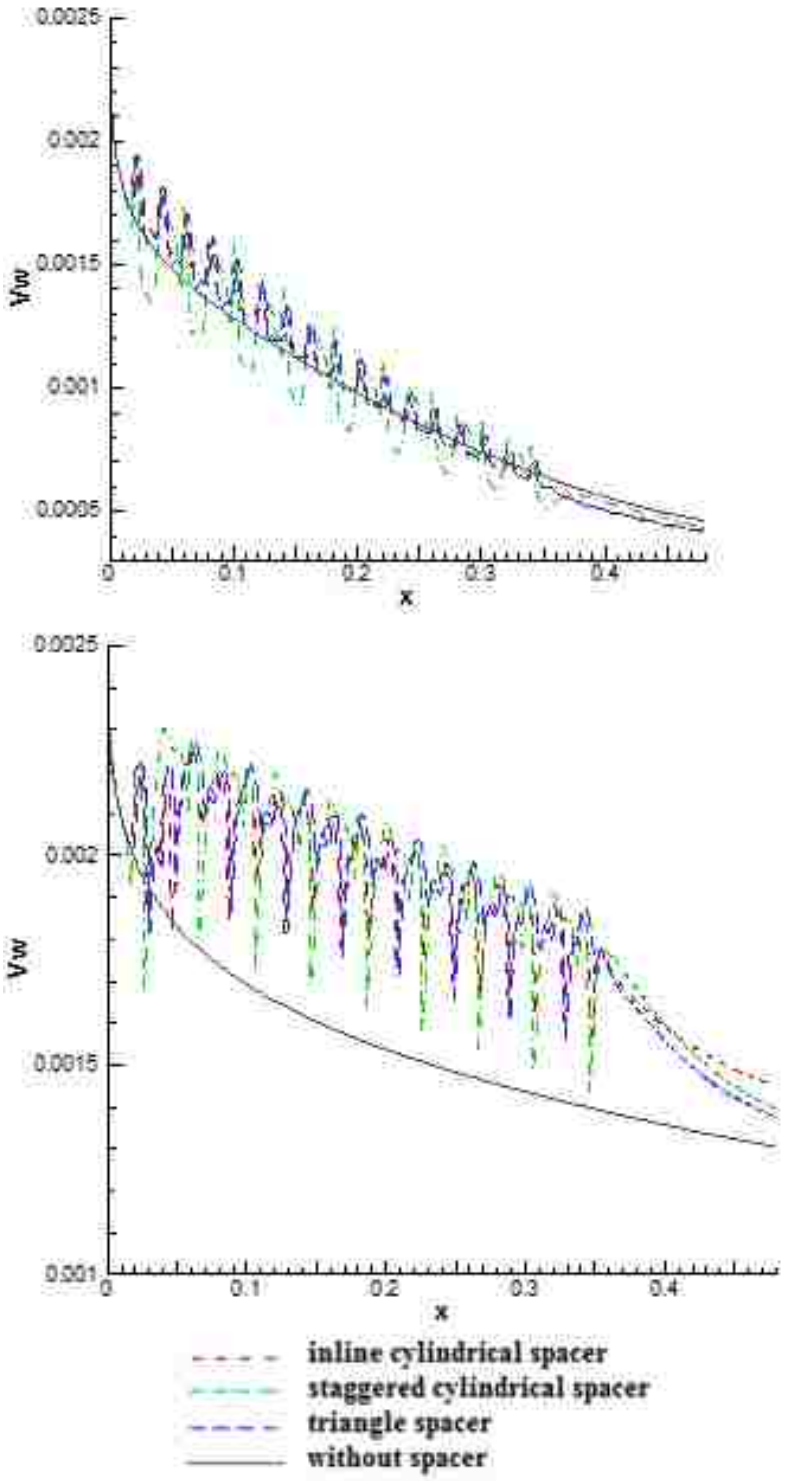

Figure 10: The suction rate along the membrane for *Re* of (a) 200 and (b) 1000.

In order to determine membrane performance, the normalized mass change of the CO_2 absorbed and the CH_4 lost is determined from

$$\Delta m_a = \frac{mass_{a,in} - mass_{a,out}}{mass_{a,in}} \quad (33)$$

where $mass_a$ is the mass of species "*a*" in a binary mixture of CH_4 and CO_2. The subscripts "in" and "out" denote the mass of each species at the inlet and the outlet of the channel.

Figure 11 depicts the normalized mass change of CH_4 and CO_2 across the channel as a function of *Re*. For comparison purposes, Figure 11 displays both the normalized mass change of the inline and staggered orientations. The mass of absorbed CO_2 and lost CH_4 for the inline and the staggered geometries with *S/d* = 10 and 5 are compared against those without the spacer. As is seen, the effect of vortex shedding on the CO_2 extracted through the membrane is captured by the time averaged representation obtained from the steady state simulations. The presence of spacers in the channel enhances the passage of CO_2 through the membrane, while reducing the percentage mass loss of CH_4 through the membrane. This clearly shows that the spacers enhance the performance of the membrane and the improvement is greater at higher value of the Reynolds number.

a)

b)

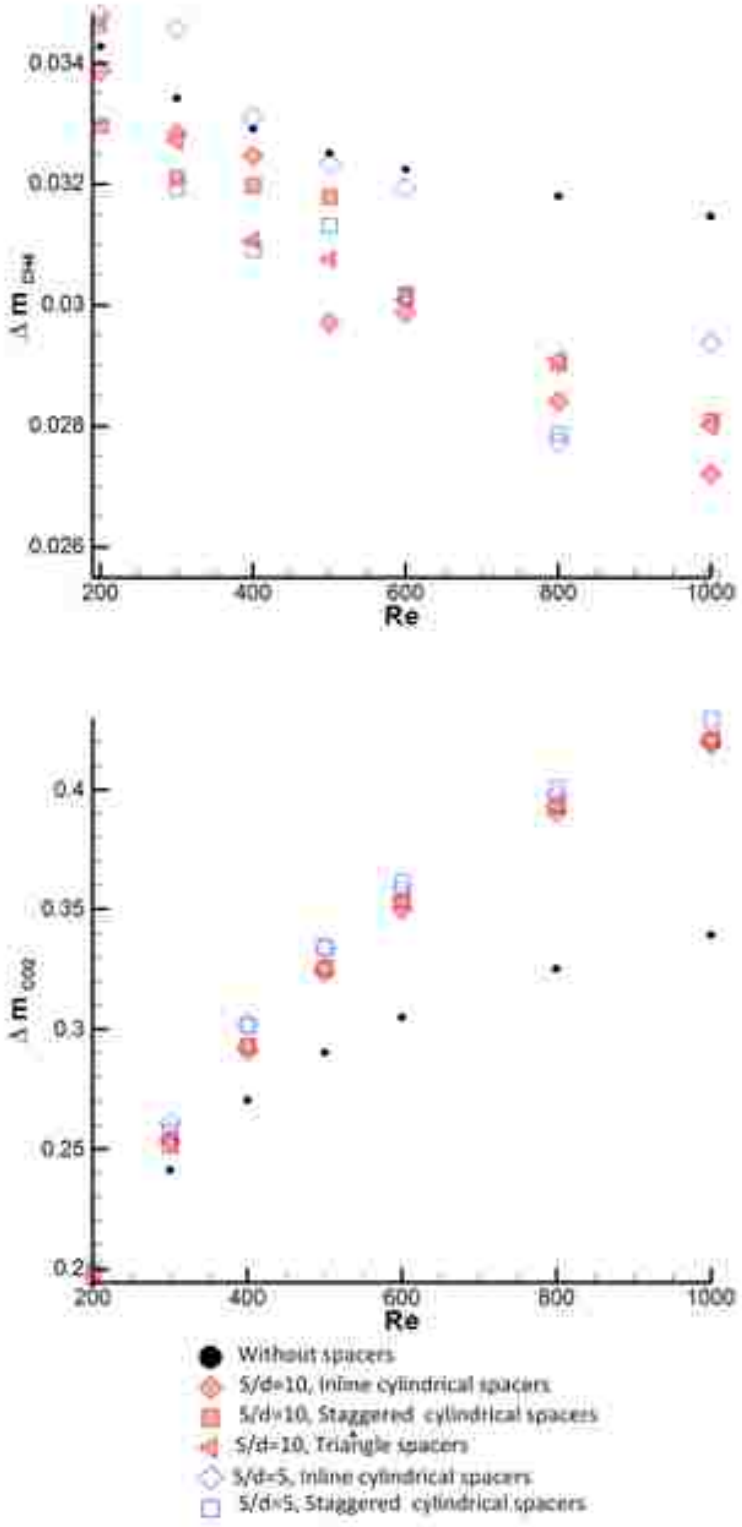

Figure 11: The normalized mass change of a) CH_4 and b) CO_2.

The Sherwood number is a better indicator of the membrane performance since it eliminates the effects of the concentration conditions selected at the inlet and the length of the test section. Figure 12 shows the local value of the Sherwood number as a function of axial position, x. The Sherwood number is calculated for the flow without the spacers and for the inline geometry of circular spacers with S/d = 10. The Sherwood number fluctuates in the flow direction with a local maxima occurring near the spacers and a local minima occurring near the midpoints between spacers. The average value of the Sherwood number in the case with spacers is more than three times greater than in the case without the spaces. This is attributed to the mixing induced by the Karman vortex street behind the spacers.

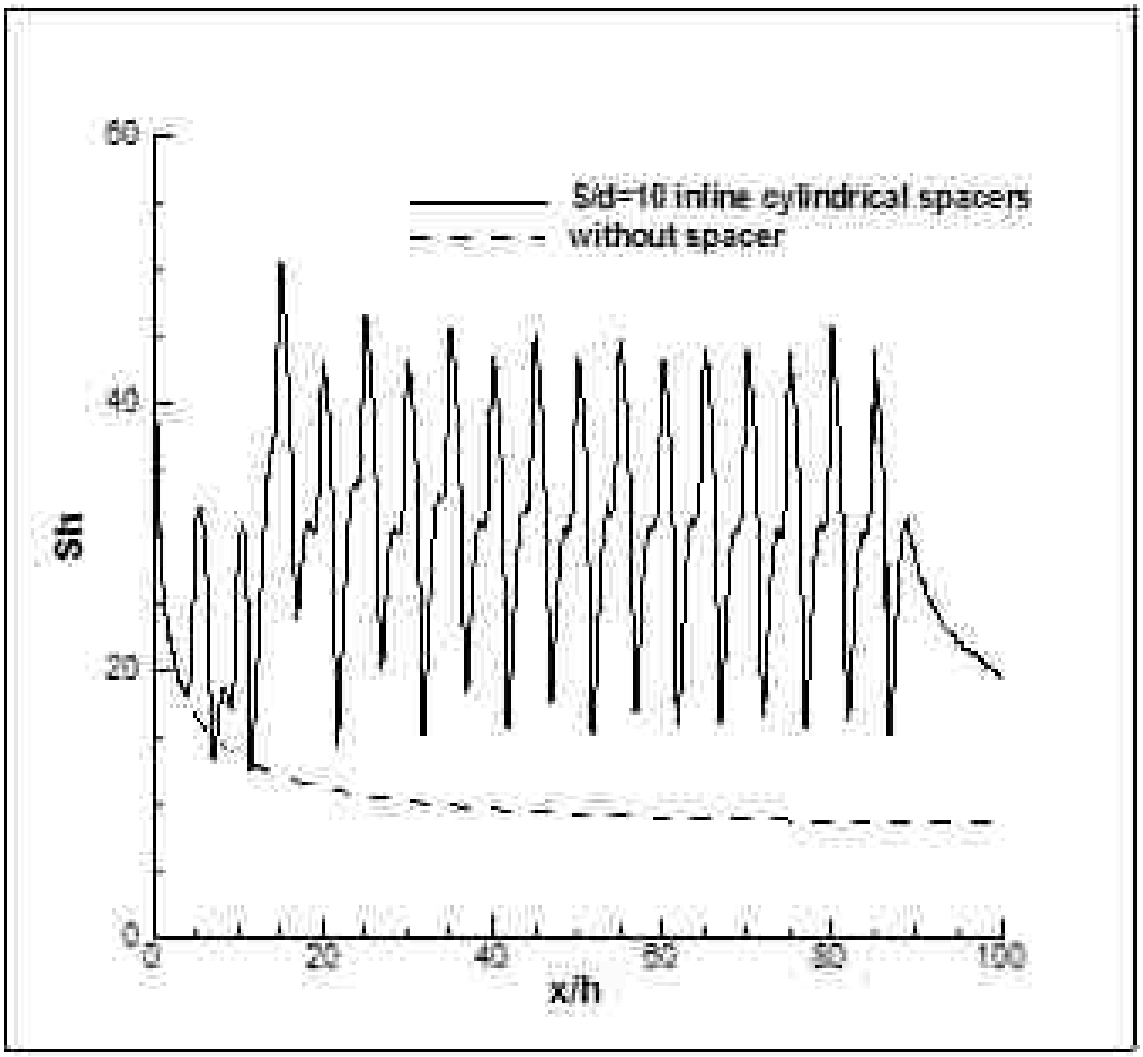

Figure 12: The local value of the Sherwood number for *Re* = 1000

Sherwood number is averaged from *x/h* 20 to 80 and plotted as a function of the Reynolds number in Figure 13. The average value of the Sherwood number in a feed channel containing spacers with the inline and the staggered arrangements are plotted and they are compared with the Sherwood number in a feed channel without spacers. The Sherwood number is elevated by the presence of spacers at all *Re*. The degree of enhancement in the membrane performance is much greater at higher *Re* flows. For both the inline and the staggered geometry, the mass transport through the membrane increases as the spacing between blockages is reduced. Also the staggered geometry provides higher mass

transport compared to the inline geometry at high Reynolds number. The shape of spacer has little influence at low *Re*, but it has a stronger influence at high *Re*. Triangular spacer leads to a higher mass flux through the membrane compared to the circular spacers at high *Re*.

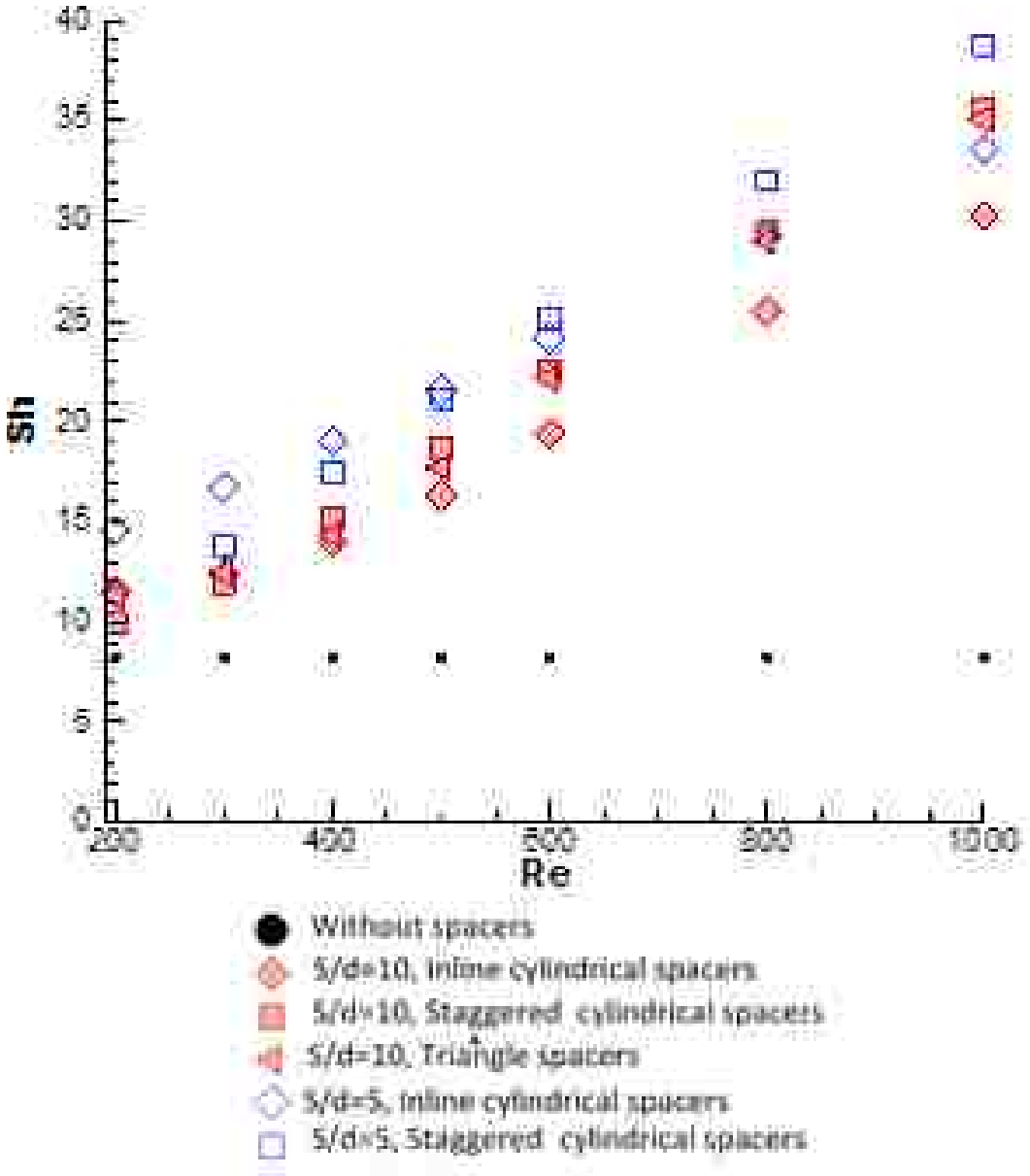

Figure 13: The Sherwood number as a function of Reynolds number

The friction factor is calculated along the surface of the membrane with and without the spacers. The average value of the friction factor as a function of the *Re* is depicted in Figure 14 for various geometries. Among the geometries considered here, the pressure drop is the highest in case of the staggered cylindrical spacers with $S/d = 5$ while it is the lowest in the case of the inline cylindrical spacers with $S/d = 10$. The operation of gas-gas separation requires a high pressure (on the order of several MPa) and the pressure of the gas leaving the separation is module is very high as well (also on the order of several MPa). The additional pressure drop caused by having spacers has no noticeable consequences (on the order of kPa). Even when the process uses an energy recovery system, the energy losses caused by the spacers will be negligible. As a result, the performance of the membrane should be measured mostly by the increase in mass flux through the membrane without major consideration of the pressure drop.

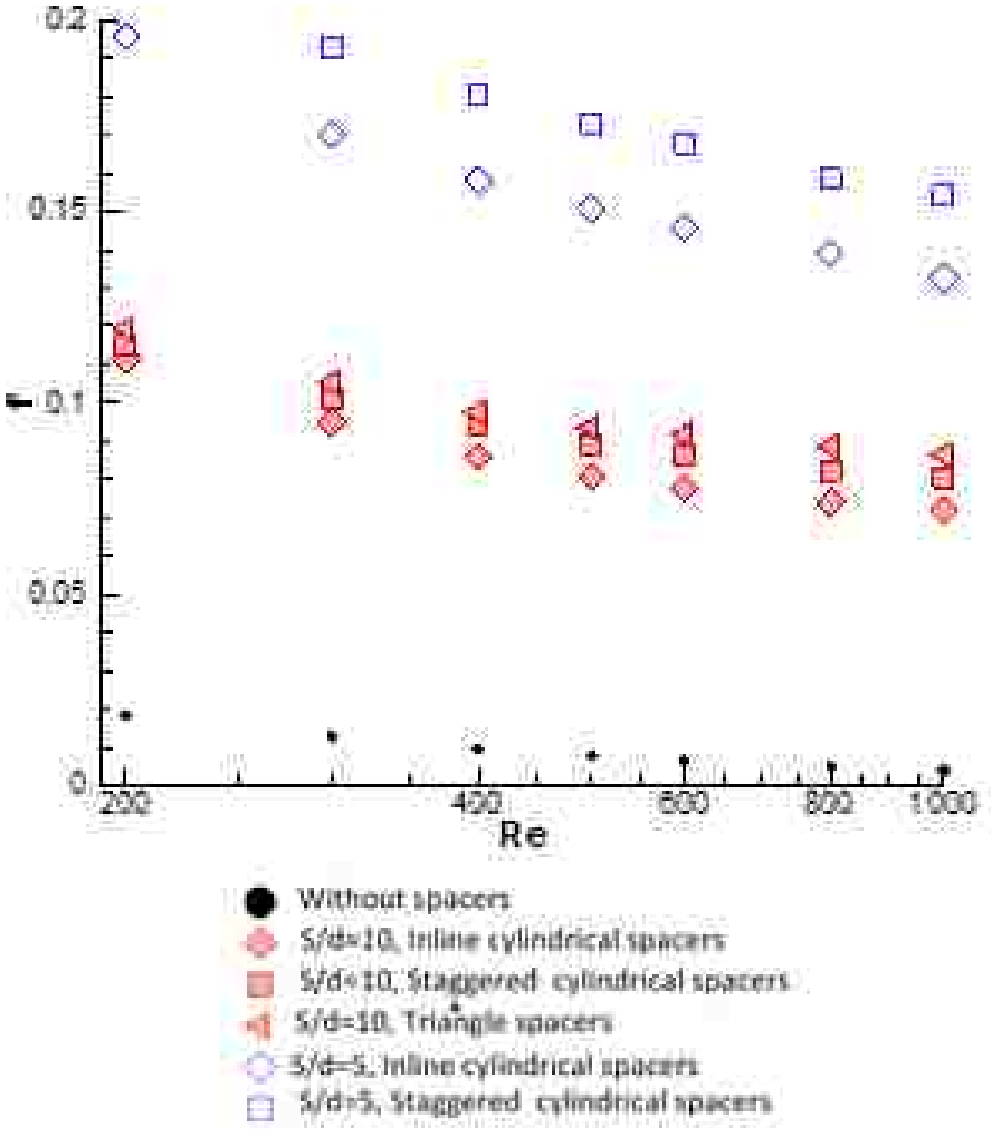

Figure 14: The averaged value of the friction factor as a function of Reynolds number

In order to understand the influence of the temporal structure of the flow on the membrane performance transient simulations are performed using transient k-ω and LES turbulence modeling for Re = 800. The flow past the circular spacers in an inline geometry with S/d = 10 is simulated. The true effects of the Karman vortex street on the

mass flux though the membrane can be determined from these simulations. LES provides more details about the flow structure produced by the Karman vortex street in the wake of the spacers. Figure 15 illustrates the velocity vectors and the contours of the CH_4 concentration at t = 0.021 s. The images are shown at various locations of the flow domain: near the first and the second cylinder (see Figure 15a1 and 15b1), near the sixth and the seventh cylinder (see Fig 15a2 and 15b2), and near the last cylinder (see Figure 15a3 and 15b3). The effect of the mixing is clearly visible in the concentration field. The velocity field is similar around all cylinders. The images clearly indicate that the mixture becomes CH_4 richer at downstream locations. The lift force signature of the first cylinder is shown in Figure 15c. The periodically shedding swirling vortices cause the lift force exerted by the fluid on the first spacer to fluctuate in time with a well-defined frequency of 668 Hz, as indicated by the power spectral density of the lift coefficient – see Figure 15d. The Strouhal number of about 0.2 predicted by both LES and the k-ω model agrees well with that measured by [61].

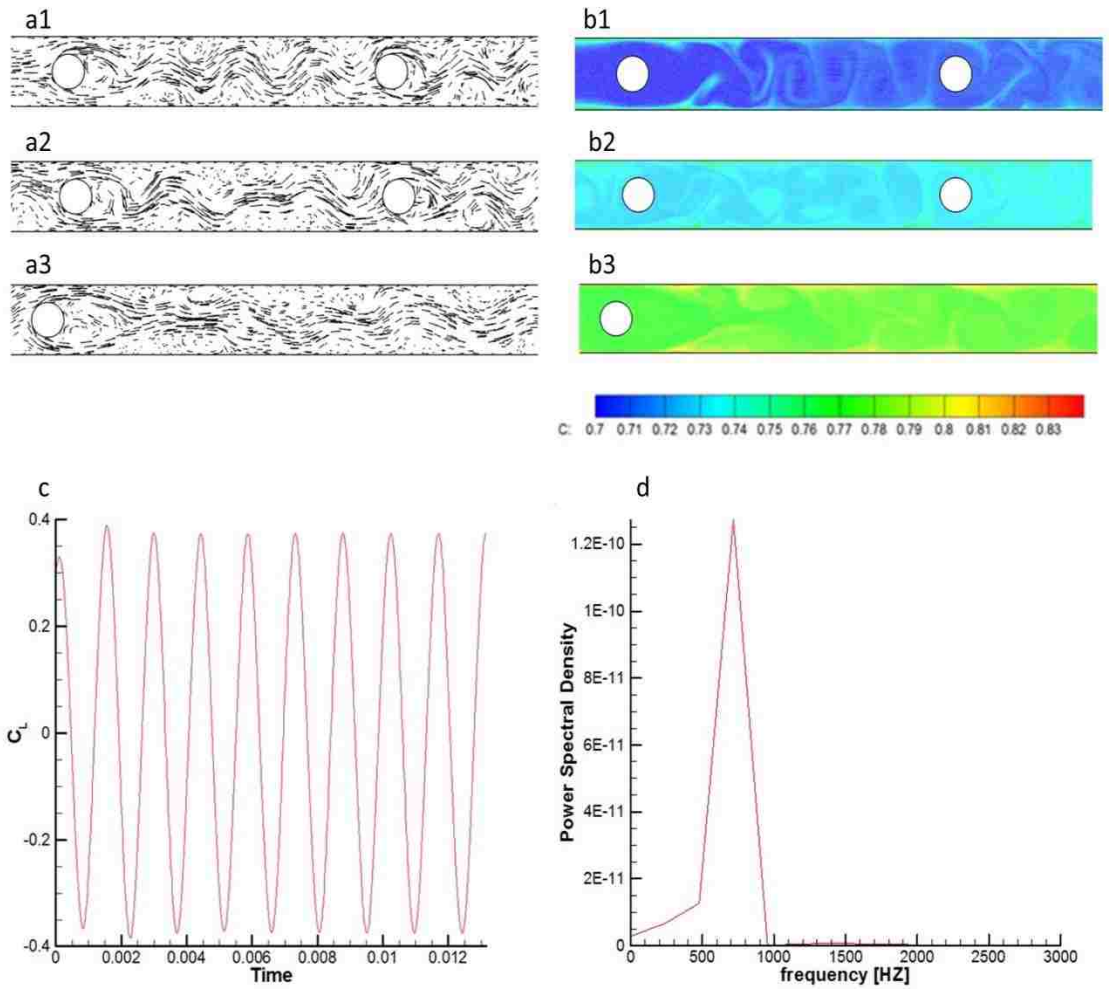

Figure 15: a) The velocity vectors, b) the contours of concentration, c) the lift force vs time and d) the power spectrum density of the lift force predicted by LES. The images are around (1) the first and the second cylinder, (2) the sixth and the seventh cylinder, and (3) the last cylinder

Figure 16 compares the local value of the Sherwood number predicted by the LES and the transient *k-ω* BSL model. The local value of the *Sh* is calculated: a downstream of the first cylinder (*x/h* = 5.5), at the midpoint between the first and the second cylinder (*x/h* = 7.5), an upstream of the second cylinder (*x/h* = 9.5). The Sherwood number,*Sh*, is plotted in Figure 16 as a function of time. Even though the *Sh* predicted by LES and the *k-ω* BSL method differs, the mass flux of CO_2 through membranes predicted by these methods agrees within 0.03%.

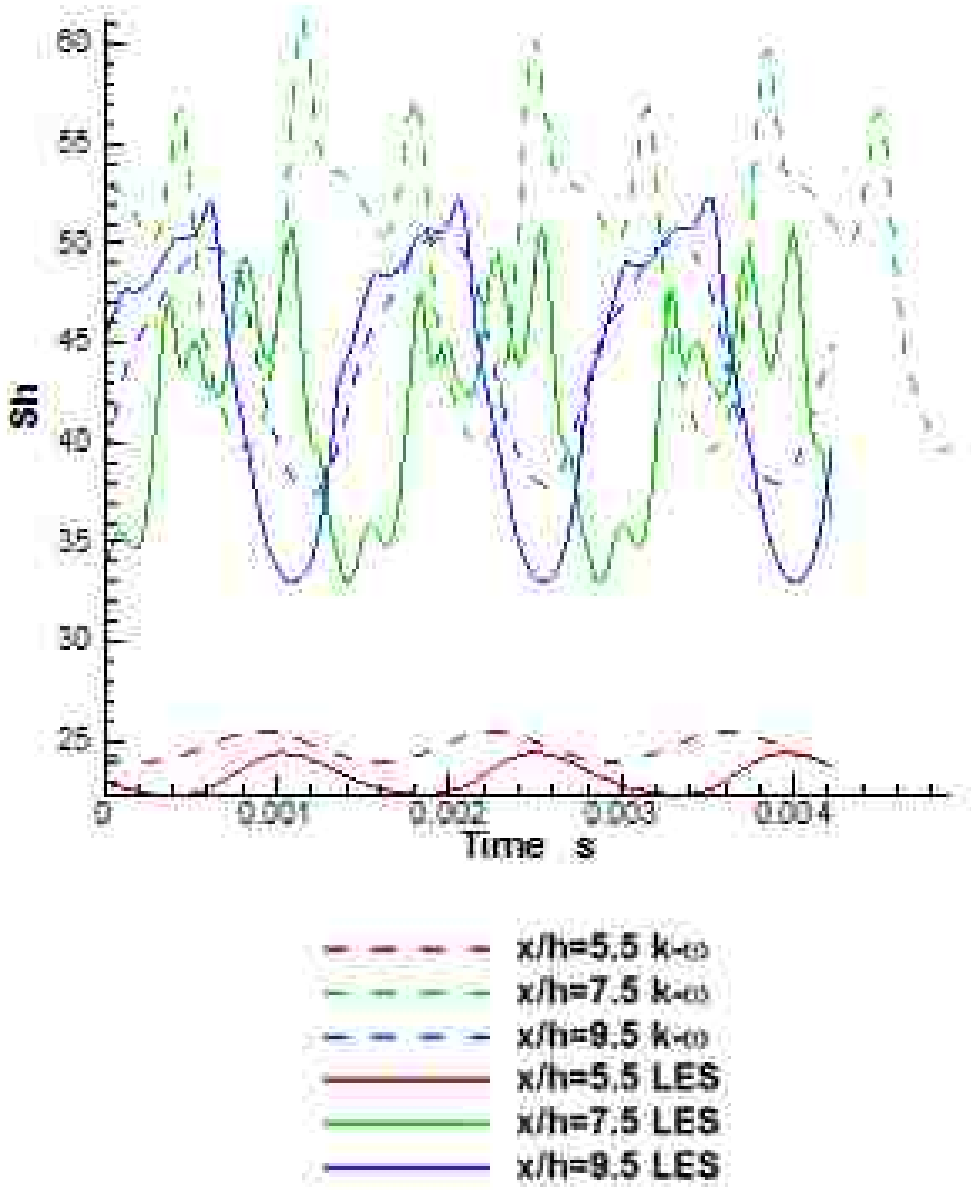

Figure 16: Sherwood Number comparison between LES and transient *k-ω* BSL

In order to understand the pulsating effect on the membrane performance, different pulsate frequency was investigated for the Reynolds number of 800. Figure 17 show the lift force exerted by the fluid on the cylinder at the first row. The fact that the frequency of the fluctuations of the lift force is nearly the same for all three cases implies

that the lift force is dominated by the vortex shedding. For no pulsation the Strouhal number is predicted to be about 0.2, which matches with those reported in the literature. These results also clearly show that the frequency of the vortex shedding is hardly influenced by the periodic flow imposed at the inlet. The Strouhal number is defined as

$$\text{Strouhal number} = \frac{f_r d}{2U_{ave}} \quad (33)$$

where f_r is the frequency of oscillations, and d is the spacer diameter.

For the pulsating and the steady flow at the inlet, suction from the membrane surface results in continual decrease of the mass flow rate through the channel. Since both membranes have the same functionality, the time-averaged velocity field is symmetric about the mid-point of the channel. The periodically alternating vortex shedding from top and bottom regions of the rear stagnation point causes flow asymmetric at any instant. Starting with the uniform 70% CH_4 concentration at the inlet, the mixture becomes richer with the CH_4 away from the inlet. Both CO_2 and CH_4 are absorbed from the mixture in the channel by the membrane. The absorption of CO_2 exceeds that of the CH_4, which leads to the richer CH_4 concentration.

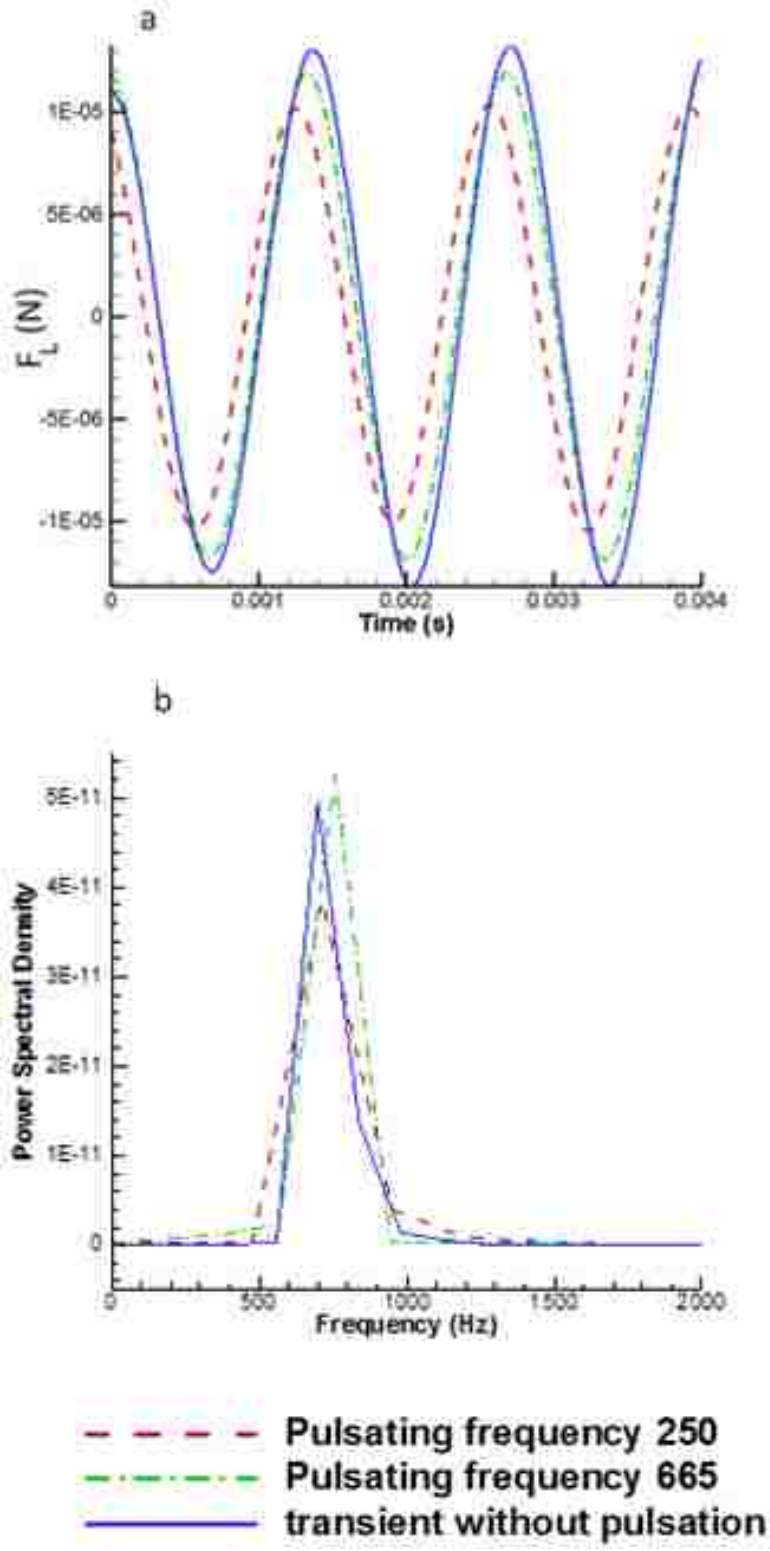

Figure 17: a) Lift force vs time and b) the power spectral density of the lift force

The velocity and concentration field near spacers are obtained by employing turbulent modeling at *Re* = 800. Figure 18 shows the velocity vectors and the contours of the concentration of CO_2. The Kármán vortex shedding is dominating the flow and concentration field in the wake of spacers. The transient simulation conducted here predicts flow structures caused by the vortex shedding from the spacer for three different pulsation frequencies (0 Hz, 250 Hz and 665 Hz). Mixing caused by the vortex shedding is expected to enhance the membrane performance.

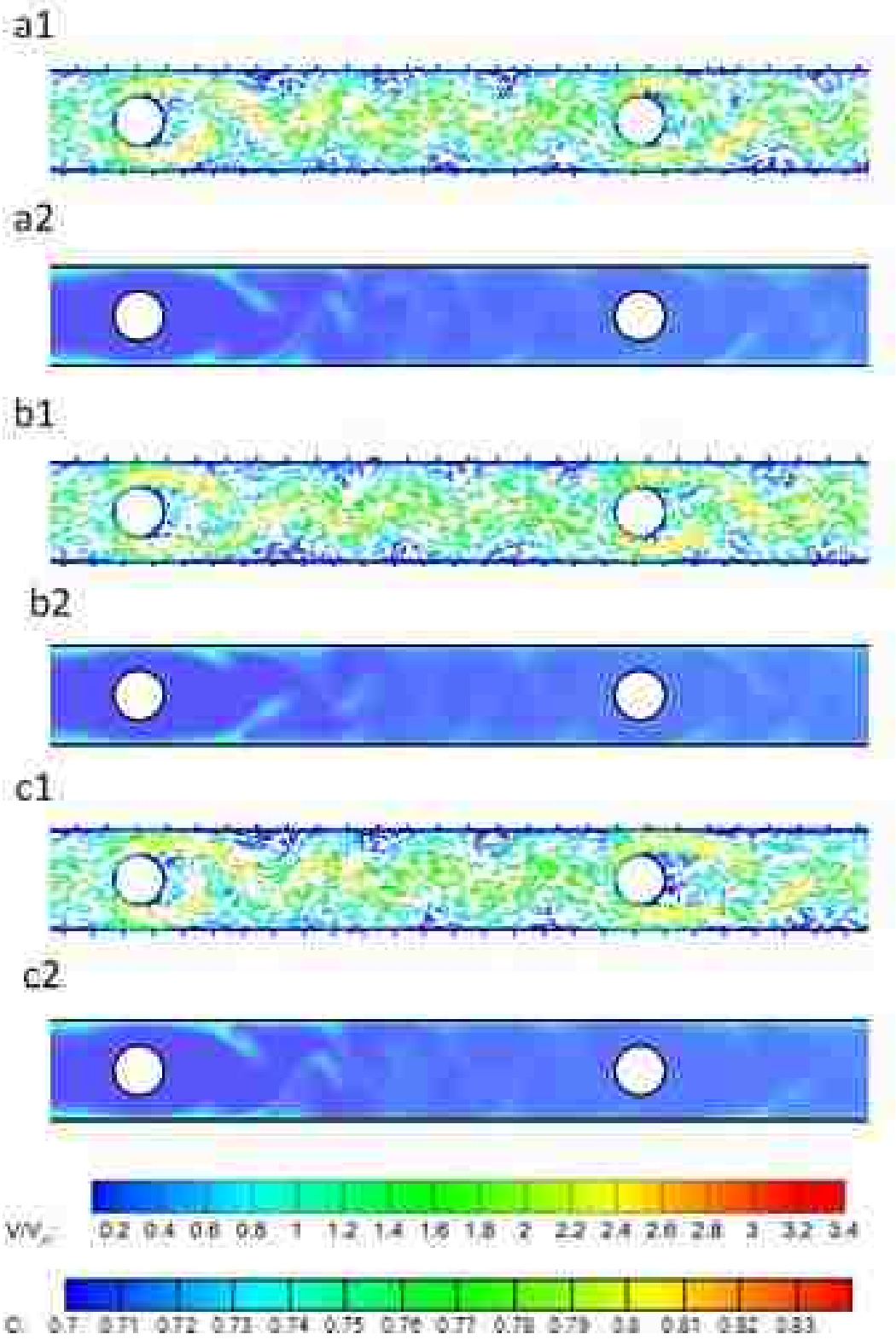

Figure 18: Velocity vectors (1) and contours of concentration of CO_2 (2) at *Re* = 800 for pulsation frequency of a) 665 Hz, b) 250 Hz and c) 0 Hz

In order to determine membrane performance, the percentage mass change of the CO_2 absorbed and the CH_4 lost is determined from

$$\%M_a = \frac{M_{a,in} - M_{a,out}}{M_{a,in}} 100 \quad (34)$$

Here M_a is the mass of species "a" in a binary mixture of CH_4 and CO_2. The subscripts "in" and "out" denote the mass of each species at the inlet and the outlet of the channel.

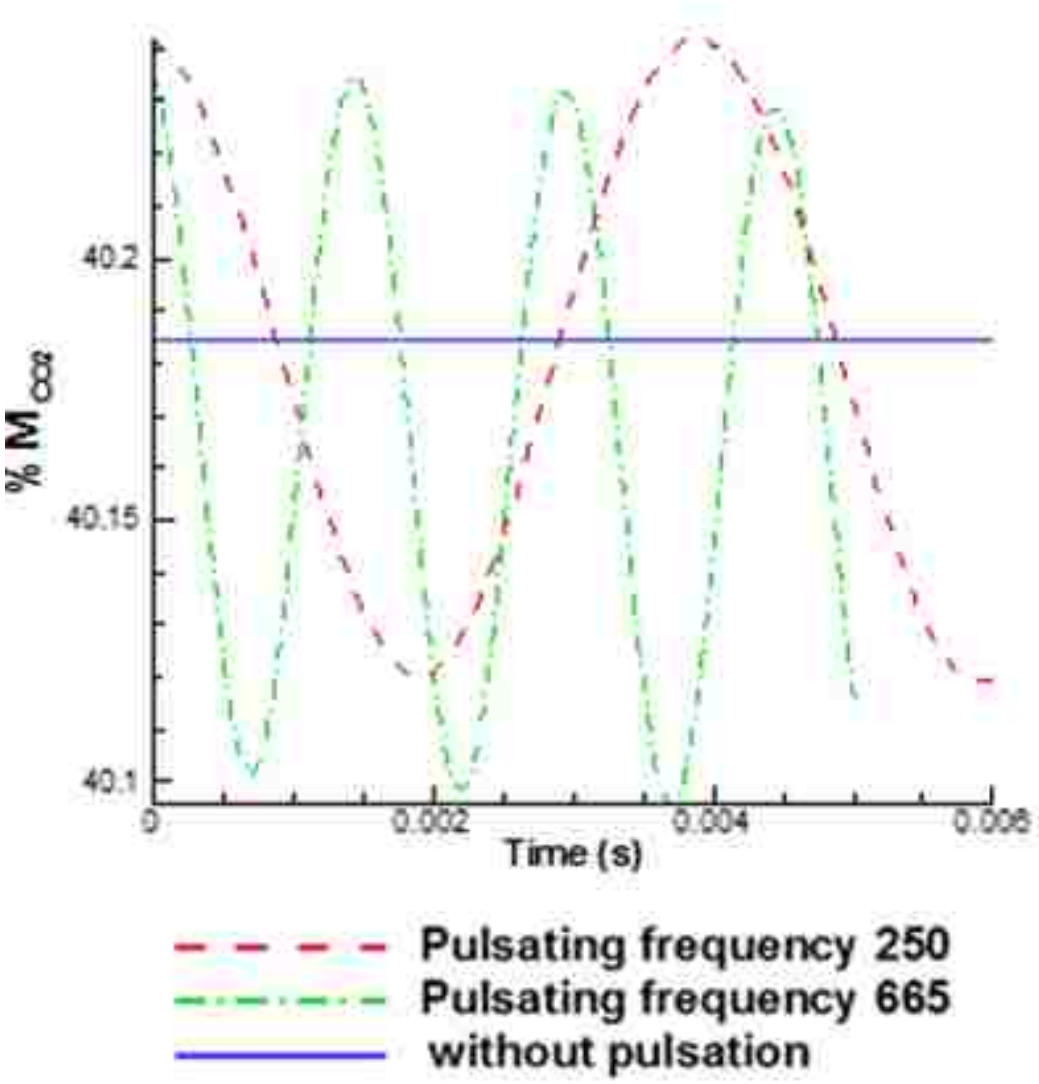

Figure 19: Percentage mass of CO_2 extracted through membrane at *Re* = 800 for different pulsating frequency at the inlet.

Figure 19 depicts the percentage change mass of CO_2 and CH_4 between the inlet and the exit of the channel for *Re* = 800 for all three pulsating frequencies. The solid line denotes the steady state and transient simulations without the pulsation at the inlet. Obviously the effects of the vortex shedding on the CO_2 extracted through the membrane are captured by the time averaged representation obtained directly from the steady state

simulations. The red and green lines in Figure 18 denote the percentage change mass of CO_2 for pulsating flow at the inlet with 250 Hz and the 665 Hz frequencies, respectively. They vary with time with the same frequency of pulsation. The average of percentage mass change is slightly lowered compared to that for no pulsation case. As the pulsation frequency increases the time average of the mass percentage decreases.

Figure 19 shows the Sherwood number right behind the first cylinder (d/x = 5.5), middle point between the first and the second cylinder (d/x = 7.5) and the right before the second cylinder (d/x = 9.5) as a function of time. The Sherwood number is periodic in time at all locations for all three cases; following the frequency of vortex shedding in each case, as shown in Figure 19. The average value of the Sherwood number right behind the cylinder is nearly the same for all cases, while the Sherwood number is higher in the middle of the cylinders and the front of the cylinders at lower frequencies. The mass flux at the surface of the membrane is strongly influenced by the nature of the vortex shedding at this Reynolds number of 800.

3.4 Conclusion

Computational fluid dynamics simulations are conducted to investigate gas-gas separation using a membrane. The CO_2 and CH_4 binary mixture is considered in the mass transport through a membrane. A unique model is presented in which the membrane is modeled as a functional surface. The mass flux of each species is determined based on the local partial pressures of each species, the permeability, and the selectivity of the membrane. Both steady and transient simulations are conducted by employing k-ω and LES turbulence modeling for *Re* up to 1000. The effect of the shape, spacing and the configuration of spacers on membrane performance is studied. The amount of CO_2

extracted increases and the amount CH_4 lost decreases when blockages are placed inside the channel. Such performance enhancement is more pronounced at higher flow rates. Staggering the spacers, increasing the frequency of the spacers, and introducing triangular shaped spacers increases the mass transport through the membrane. The pressure drop increases with the spacers, but such increase in the pressure drop is very small compared to the operating pressure of the membrane. Hence, its effect on the membrane performance is not significant. This study shows that spacers should be an important part of membrane systems used in gas-gas separation. Pulsating flows have minimal effects on the membrane performance. The average mass percentage of each species across the membrane module in pulsating flow is similar to that in steady flows. Pulsation does not influence the Karman vortex street patterns and flow induced by such vortices. Mixing caused by the Karman vortex street still dominates in pulsating flows with different frequencies.

Chapter 4: HOLLOW FIBER MEMBRANE

Two different two-dimensional flow geometries are studied in a hollow fiber membrane module: uniformly spaced orifices and uniformly spaced diffusers. The purpose of using flow restricting devices such as orifices or diffusers is to promote momentum mixing in the feed channel and in the porous layer. The results presented in this chapter was presented in [62, 63]

4.1 Hollow fiber membrane module containing orifices:

4.1.1 Problem description:

The schematic of the two-dimensional flow geometry for the hollow fiber membrane module containing orifices is illustrated in Figure 20. It consists of an open tubular channel surrounded by a porous layer which is bounded by a dense membrane. The diameter of the open tubular channel is D_1 and the diameter of the module consisting of the porous support layer is D_2, as shown in Figure 20. Uniformly spaced orifices are placed in an open channel. The diameter of the orifice is $d = 0.5\ D_1$ and the spacing between two consecutive orifices is S. The binary mixture of CH_4 and CO_2 is treated as an incompressible fluid with uniform physical properties. The flow is axisymmetric and isothermal. The diffusion coefficient is assumed to be independent of the concentration. The permeability of the porous layer is constant. The porous layer is considered to be saturated and the membrane selectivity and permeability are assumed to be constant.

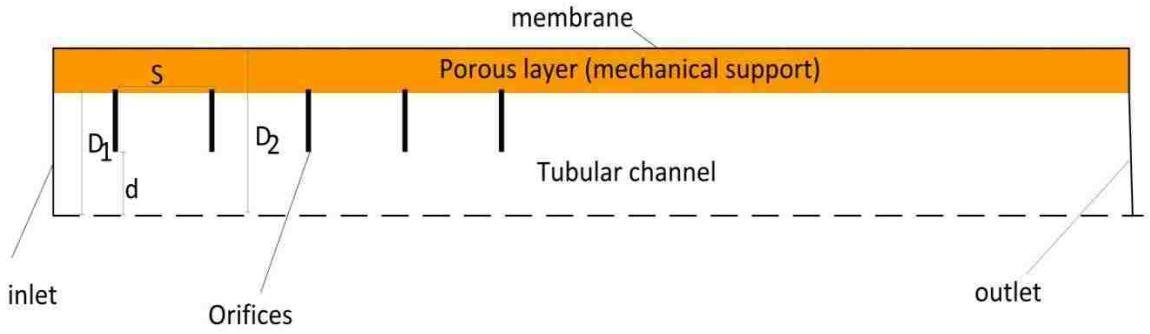

Figure 20: Schematic of the flow geometry and the membrane module

4.1.2 Method validation:

Additional validation test for the BSL Reynolds Stress turbulence model is conducted. Simulations for flow past orifices at *Re* of 100 and 300 are performed and the discharge coefficient is calculated and compared against the experimental results reported by Johansen [64]. Predicted discharge coefficient matches with measured discharge coefficient, as listed in Table 2. It is demonstrated here again that BLS Reynolds turbulence model captures the flow characteristics well for the range of Reynolds number considered here.

Reynolds number	C_d BLS	C_d experimental work by [64]	% Different
100	0.86	0.78	8.23
300	0.79	0.73	7.60

Table 2 Discharge coefficient predicted by BLS Reynolds stress model and measured by Johansen[64] at *Re* =100 and 300.

4.1.3 Results:

Results are presented in terms of the Reynolds number of the simulations to determine the inlet concentration and the radial velocity profiles. Table below shows *Re*

at the inlet for simulations with orifices as a function of the Darcy number and the inlet Reynolds number of the simulations without orifices. Reynolds numbers of the orifice simulations are slightly lower than those used to determine inlet conditions, as shown in Table 3.

Re-simulations for inlet conditions	**Re – simulations with orifices**		
	Dp* = 3.7	**Dp* = 0.37**	**Dp* = .037**
100	96.5	97.9	98.1
150	147.5	147.8	148.8
200	197.9	197.9	198.3
250	247.1	247.4	248.9
300	297.3	298.9	298.5
350	348.1	348.8	348.5
400	397.8	397.6	398.4

Table 3: Reynolds number of the simulations with orifices for various values of Darcy number.

Baseline Reynolds Stress turbulence model is used for the range of the Reynolds number considered in this study, $100 \leq Re \leq 400$. The steady flow simulations in the complex membrane module are attempted by employing laminar model. Steady laminar flow simulations did not produce converging results for $100 \leq Re \leq 400$. On the other hand, transient laminar flow simulations with time step of 8.1×10^{-6} produces converged steady results. Spatial resolution used in the transient simulations is not sufficient to predict small and large scale eddies if present in the flow domain. Figure 21 depicts the

time-averaged flow properties predicted by the transient laminar model after 300,000 time steps and the steady Baseline Reynolds Stress turbulence model at *Re* = 400. Profiles of the axial component of the velocity, the radial component of the velocity and the mole fraction are plotted at various cross-sections. Also plotted is the normalized suction rate along the membrane surface. Profiles predicted by each method are nearly the same. This proves that the turbulence model employed here accurately predicts the velocity and the concentration field and the membrane flux. The Baseline Reynolds Stress turbulence model is proposed to simulate flows having both turbulent and laminar flow regimes. Transient laminar flow simulations could be used for all the results presented here, but it uses computational time ten folds greater compared to that of steady Baseline Reynolds Stress turbulence model.

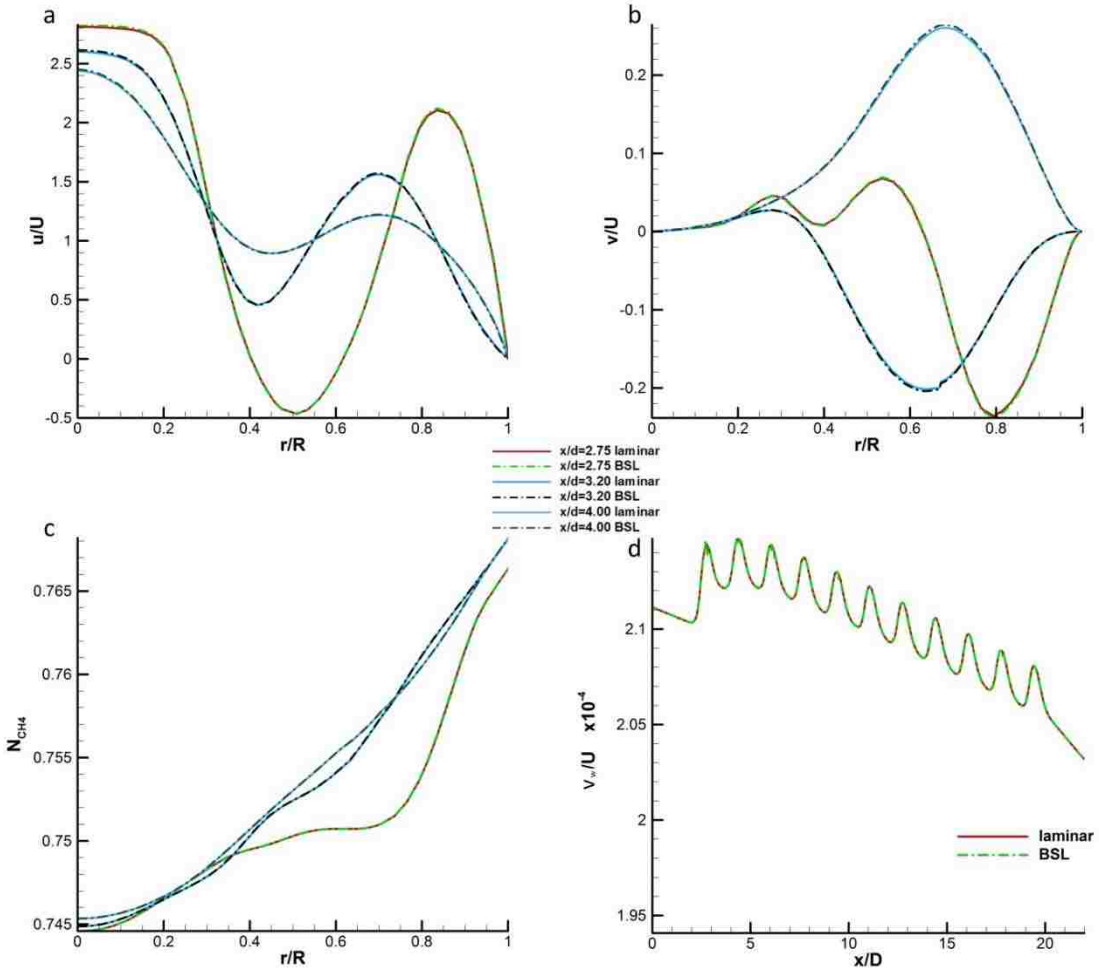

Figure 21: Profiles of a) the axial component of the velocity, b) the radial component of the velocity, c) the mole fraction at various cross sections and d) the suction rate along the membrane surface. Results are obtained by employing transient laminar flow model and the Baseline Reynolds Stress turbulence model at *Re* = 400.

Figure 22 depicts the steady state stream-wise component of the velocity and the concentration of CH_4 contours around first two orifices for *Re* = 400 and *S*/*d* = 10. The images are shown for three different values of dimensionless permeability of porous layer (the Darcy number), *Dp**. The orifices restrict flow in the open channel and direct it into the porous layer, as shown in Figure 22. As porous layer becomes less permeable

intensity of the flow through the porous layer decreases while the intensity of the flow near the center of the tubular channel increases. Fluid migrates from the porous layer to the open channel after passing the orifice since it follows a minimum resistance path. The intensity of the migration from the porous layer to the open layer increases as the permeability of the porous layer decreases. Such flow patterns are repeated after each orifice. These flow structures induced by orifices have strong influence on the concentration field, as illustrated in Figure 22. The momentum mixing, caused by the orifices, not only affects the distribution of the concentration but also influence the mass flux through the membrane. The membrane performance is expected to be improved by the induced momentum mixing.

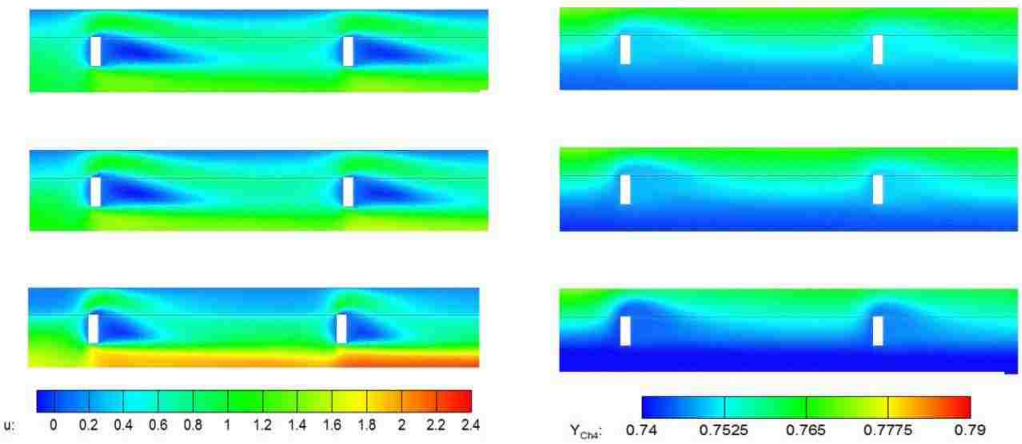

Figure 22: The steady state contours of the stream-wise component of the velocity and the concentration of CH_4 for *Re* = 400 and *S/d* = 10. Images on the left denote the contours of the velocity field and images on the right denote the contours of concentration field. Images from top to bottom are for *Dp=3.7, *Dp**=0.37, and *Dp**=0.037, respectively.**

Figure 23 illustrates the steady state contours of CH_4 concentration at upstream and downstream sections of the hollow fiber membrane module for *Re* = 400 and *Dp** =

3.7 in all three geometries. The mixture becomes CH_4 richer as it flows through the membrane module, as shown in Figure 23 in all three geometries. The momentum mixing induced by the presence of the orifice clearly promotes concentration mixing. The radial concentration stratification is significantly greater in the membrane system without the orifice compared to those containing orifice, as depicted in Figure 23. The mean concentration of CH_4 is calculated at cross-sections situated at the upstream and the downstream sections in all three geometries. The upstream cross-section situated at location that is right after the first orifice while the downstream cross section situated at location that is right behind the last orifice. The mean concentration is about 0.755 at the upstream cross-section in all three geometries. The mean concentration at the downstream cross-section is 0.771, 0.768 and 0.760 for S/d = 10, 20 and the geometry without orifices, respectively. The presence of orifice improves separation through the membrane. The increase in CH_4 concentration through the membrane module is not as high since the hollow fiber membrane module considered in the present study has a short length. Such short length membrane module is selected to make simulations feasible.

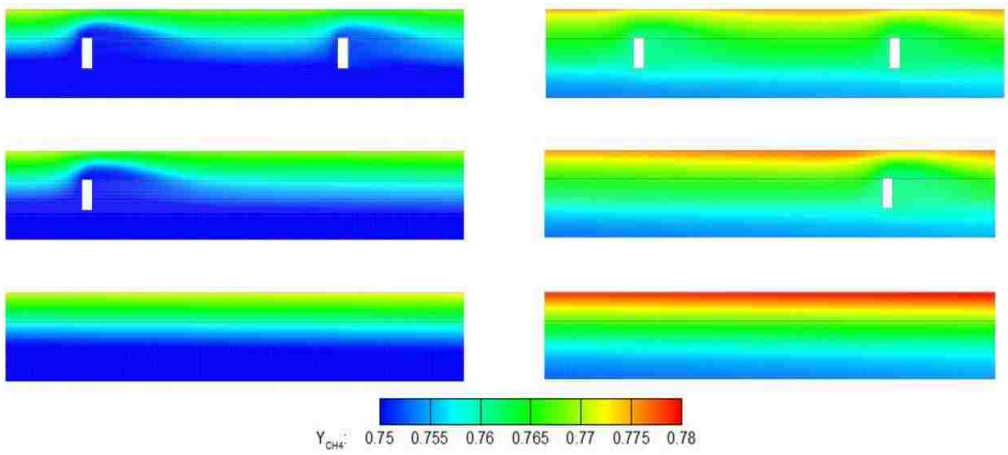

Figure 23: The steady state contours of the concentration of CH_4 for Re = 400 and Dp^*= 3.7 in three geometries. Images at the top, middle and the bottom rows are for S/d = 10, S/d = 20 and the hollow fiber membrane without orifices, respectively. Images on the left denote the contours at the upstream section of the membrane system ($2 \leq x/D_2 \leq 5$) and the images on the right denote the contours at the downstream section ($17 \leq x/D_2 \leq 21$).

Figure 24 shows the suction rate along the membrane at Re = 100 and 400 for three different values of the Darcy number, Dp^*. The suction rate profiles are shown for S/d = 10 and 20 and for a hollow fiber membrane module that is not containing orifices. The suction rate along the membrane increases as Re is increased in all geometries. There is no discernible change in the suction rate as the permeability of the support layer is varied in the membrane module without the orifices, as illustrated in Figure 24. The influence of the orifice on the mass flux through the membrane is more pronounced in the membrane module with low permeability support layer, as shown in Figure 24. It is also noticed that the effect of orifices on the mass flux through the membrane is more profound at higher flow rate. The tighter spacing of orifices (S/d = 10) increases the suction rate slightly more compared to that of S/d = 20, as illustrated in Figure 24.

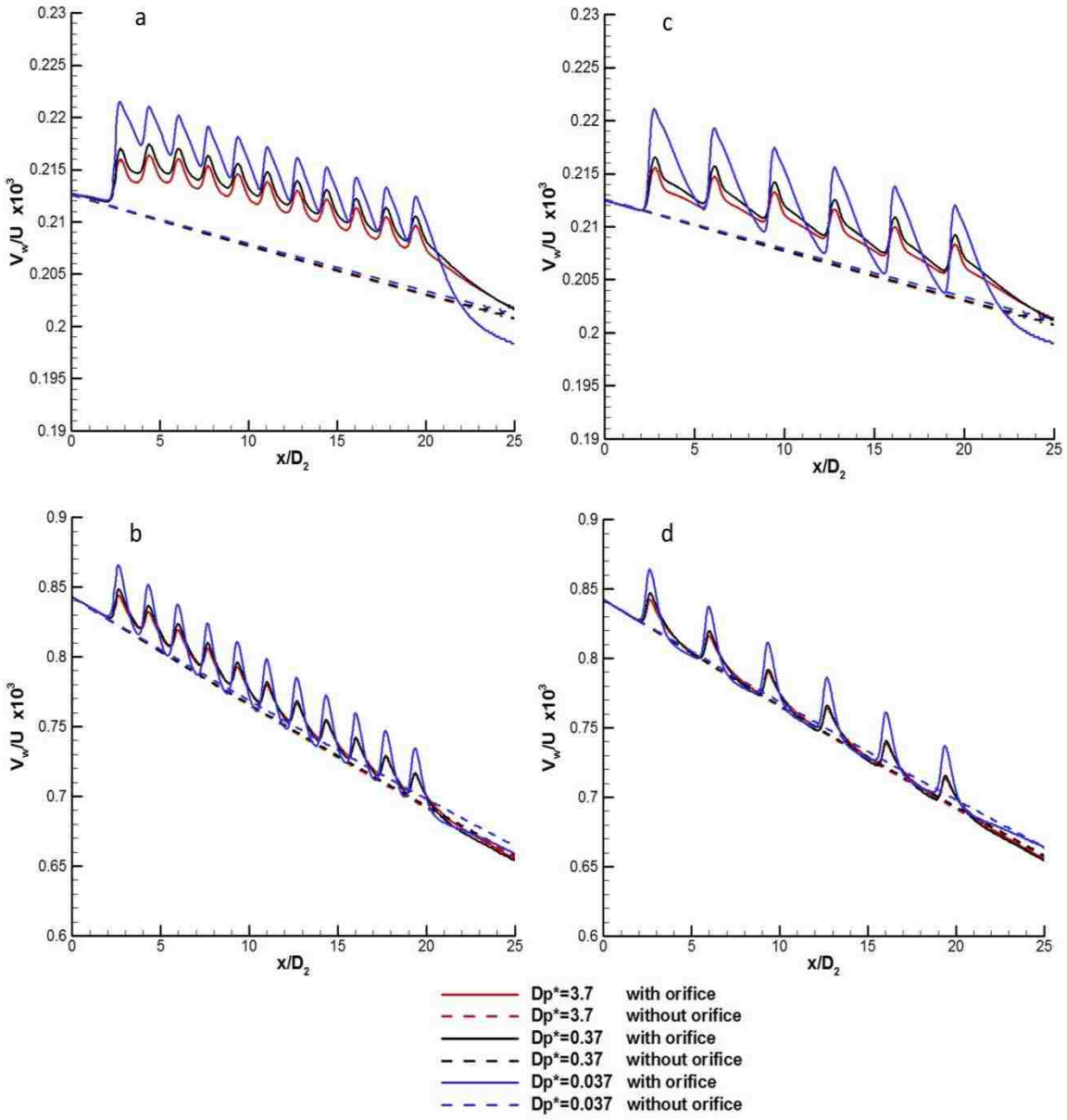

Figure 24: The suction rate along the membrane for (a) *Re* = 400, *S*/*d* = 10, (b) *Re* =100 *S*/*d* = 10, (c) *Re* = 400, *S*/*d* = 20 and (d) *Re* = 100, *S*/*d* = 20.

Figure 25 shows the local value of the Sherwood number as a function of x at Re = 100 and 400 for S/d = 10 and 20. In order to assess the effect of the orifice on the membrane performance the Sherwood number, Sh, is normalized by the Sherwood number of the membrane module without orifices, Sh_0. The value of the normalized

Sherwood number, Sh/Sh_0, above unity indicates that the mass flux through the membrane is improved by the placement of the orifice in the feed channel. The Sherwood number fluctuates in the flow direction with a local maxima occurring near the orifices and the local minima occurring near the midpoints between orifices. The value of the local maxima increases and the value of the local minima decreases as the permeability of the porous layer decreases. The effect of the orifice on the hollow fiber membrane performance is strongly dependent on the properties of the support layer, as shown in Figure 25. It is also important to note that the influence of the orifice on the membrane performance is also strongly dependent on the flow rate or *Re*. The spacing of orifices has significant influence on the Sherwood number, especially at higher flow rate. This result proves that careful selection of the orifice spacing is necessary in the optimization process of the hollow fiber membrane design.

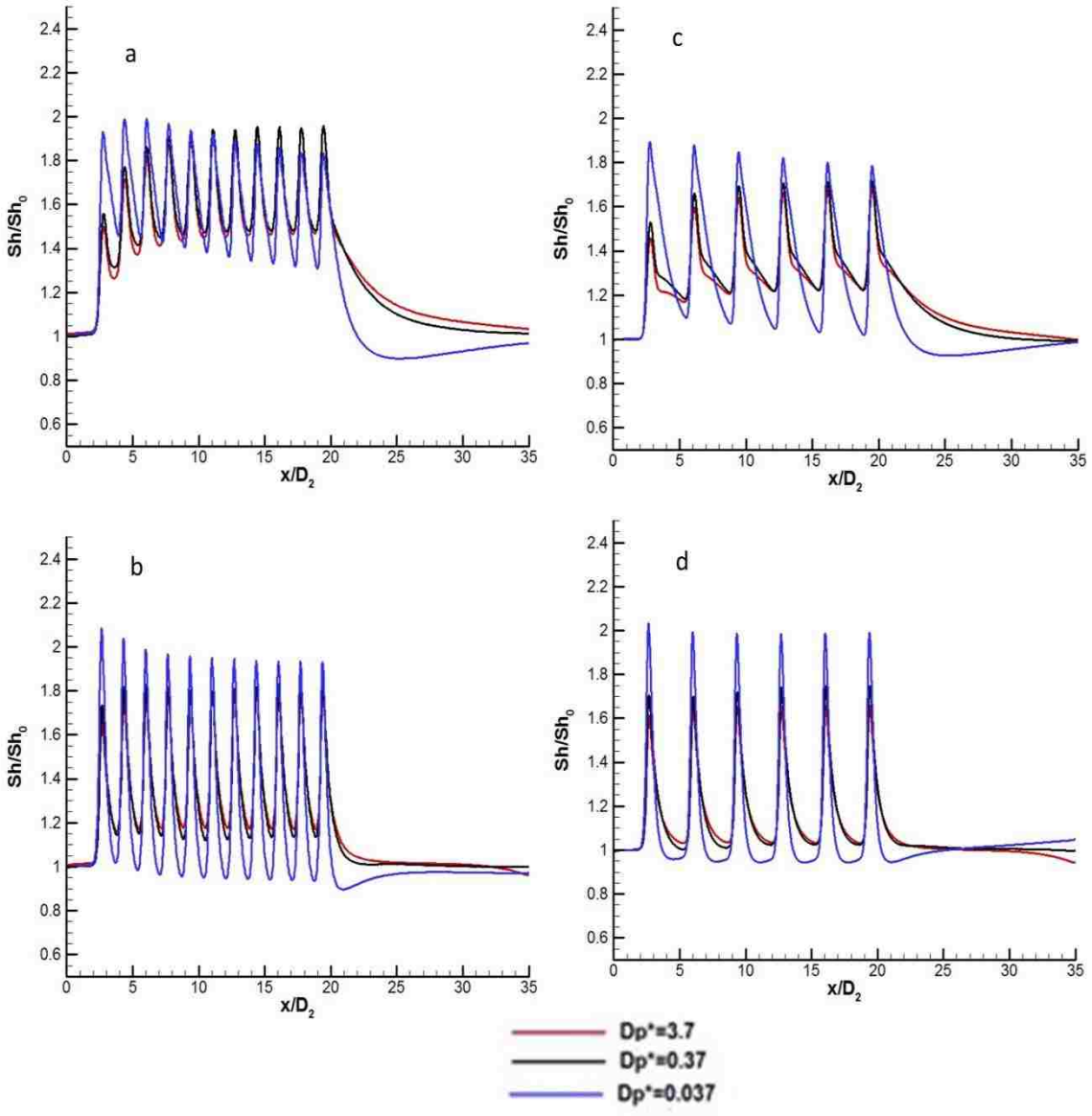

Figure 25: The normalized local value of the Sherwood number vs x/D_2 at (a) Re =400, S/d =10, (b) Re =100 S/d =10, (c) Re =400, S/d =20 and (d) Re=100, S/d =20.

The average value of the Sherwood number is calculated and is plotted in Figure 26 as a function of *Re* for *S*/*d* = 10 and 20. The average value of the Sherwood number is determined from the local value from *x*/*d* of 10 to 25. The Sherwood number is raised by the presence of orifices at all Reynolds number for both geometries with *S*/*d* = 10 and 20.

The enhancement in the performance of the hollow fiber membrane is greater at higher *Re* in both geometries, as depicted in Figure 26. The degree of the improvement is much less in the module with low permeability support layer, as seen in Figure 26 for *Dp** = 0.037. The effect of the orifice on the membrane performance is very similar for *Dp** of 0.37 and 3.7 in each geometry. The influence of the porous layer is more pronounced at low flow rates. The increase in the average Sherwood number with the presence of orifices is up to 60% in the geometry with *S*/*d* of 10 and is up to 35 % in the geometry with *S*/*d* of 20.

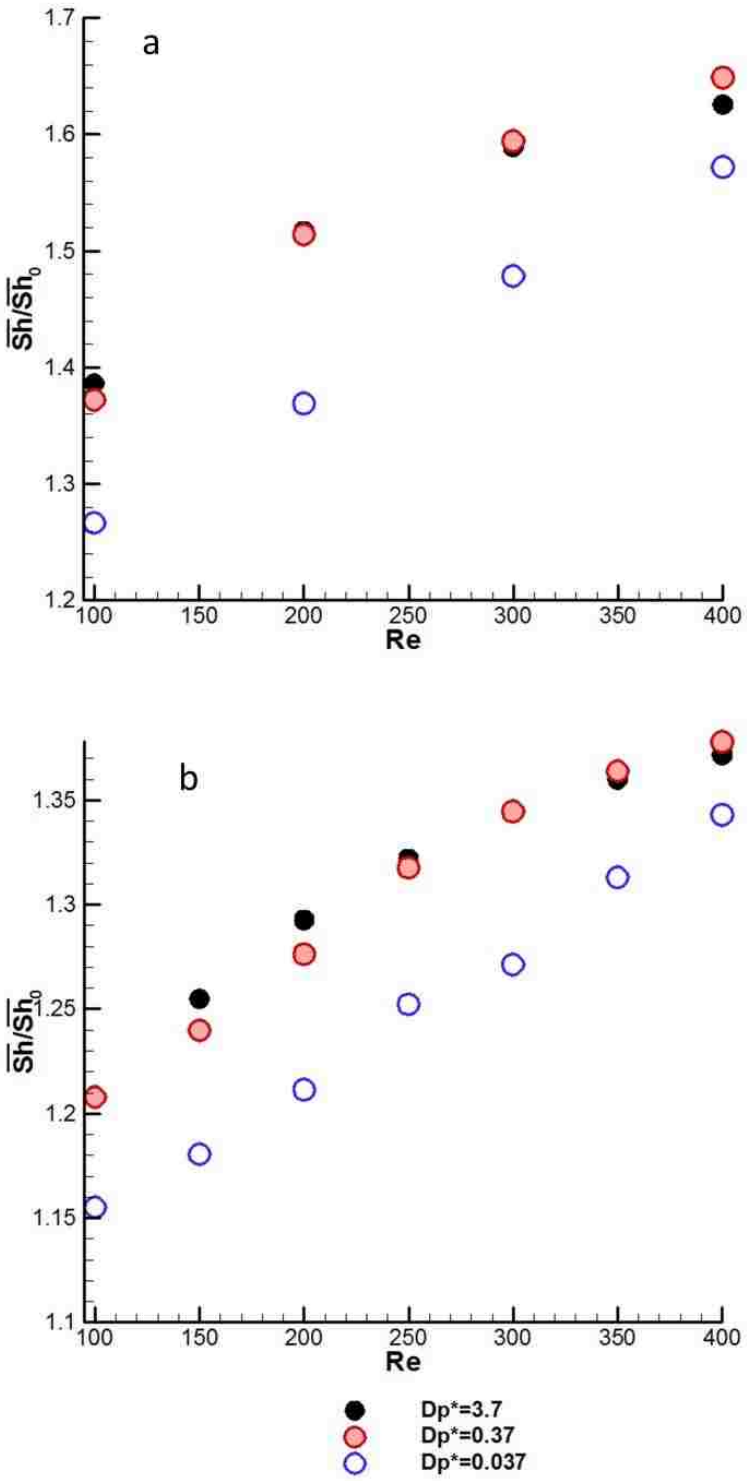

Figure 26: The normalized Sherwood number averaged over the membrane module plotted as a function of the Reynolds number for *S/d* of (a) 10 and (b) 20

The friction factor in the hollow fiber membrane with and without orifices is calculated. The average value of the normalized friction factor as a function of *Re* is plotted in Figure 27. The friction factor in the membrane with the orifices is normalized by the friction factor without the orifices. The friction factor increases three-four folds when the orifices are introduced to the hollow fiber membrane in the geometry with S/d = 20. The friction factor is four to seven times higher in the geometry with S/d = 10. The increase in the energy losses is higher as flow rate is increased, as shown in Figure 26.

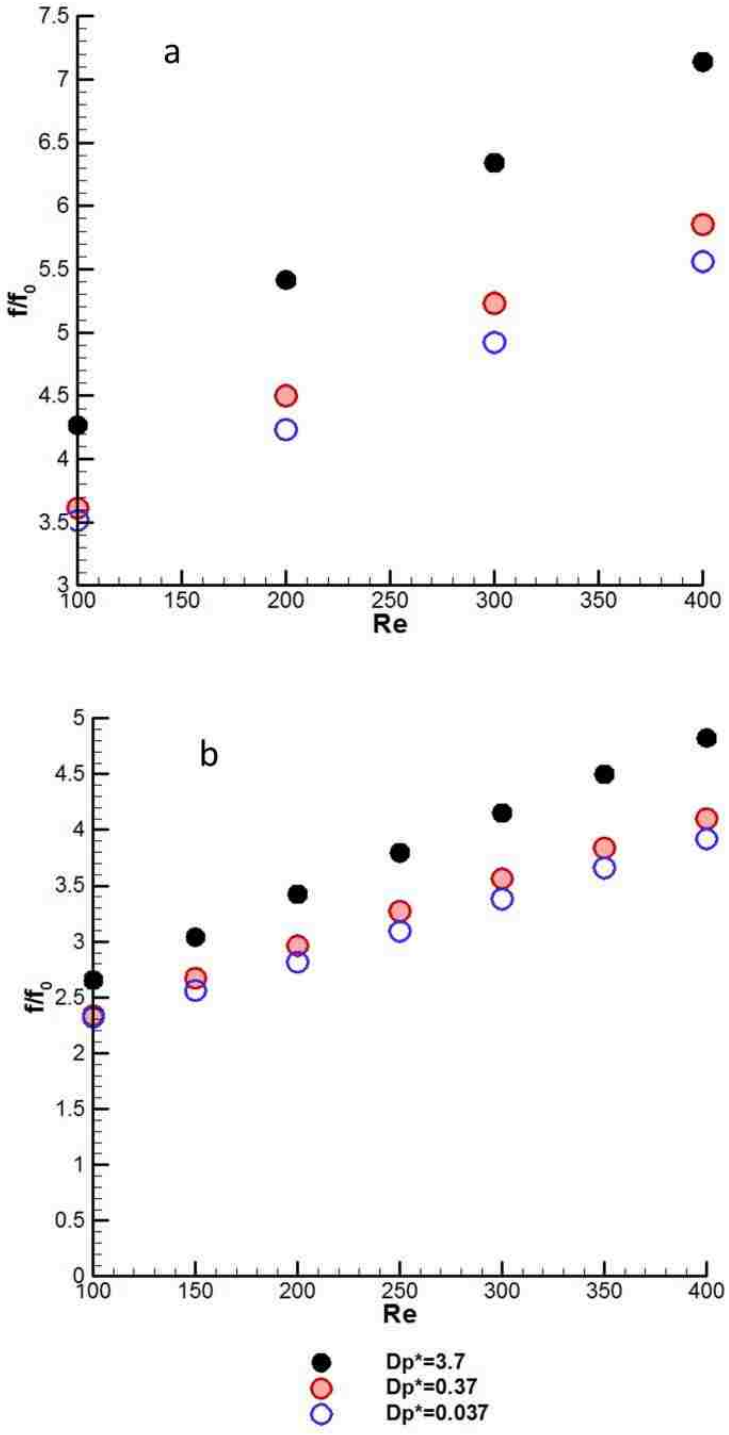

Figure 27: The averaged value of the friction factor as a function of the Reynolds number for *S/d* of (a) 10 and (b) 20

The merit number can be introduced to determine the efficiency of orifices in separation process. The merit number based on the membrane enhancement for the same power usage can be written as $(Sh/Sh_0)/(f/f_0)^{1/3}$. Values of the merit number are listed in Table 4 at various values of the Reynolds number and the Darcy number for S/d = 10 and 20. Merit number for all cases are slightly below unity; implying that placing orifices in the hollow fiber membrane modules would not be an efficient option. However, this should not deter the use of orifices in gas-gas separation process considered here. The operation of gas-gas separation requires a high pressure (on the order of several MPa) and the pressure of the gas leaving the separation module is very high as well (also on the order of several MPa). The additional pressure drop caused by having orifices may not be a factor. The magnitude of the pressure drop in the membrane with orifices is at the level of about 100 Pa per meter at low *Re* and about 1 kPa per meter for high *Re* flows. It should also be mentioned that this study consider only one size of the orifice in different spacing. Further study should be conducted to better understand the efficiency of orifices with different sizes and different configurations.

$S/d = 10$				
		Dp^*		
		3.7	**0.37**	**0.037**
Re	**100**	0.854765	0.894353	0.833127
	200	0.863815	0.917079	0.846581
	300	0.858729	0.91851	0.869242
	400	0.844391	0.914764	0.88749
$S/d = 20$				
		Dp^*		
		3.7	**0.37**	**0.037**
Re	**100**	0.873126	0.909885	0.872388
	150	0.866277	0.893503	0.862883
	200	0.857604	0.888546	0.858096
	250	0.847522	0.88773	0.859723
	300	0.83611	0.880281	0.847162
	350	0.823861	0.871008	0.852138
	400	0.811803	0.860986	0.851742

Table 4: Merit numbers of orifice enhancement for two orifice spacing *S*/*d* of 10 and 20. Merit numbers are listed for various values of the Reynolds number and the Darcy number.

Nevertheless, the pressure drop or the energy loss due to friction should be considered in the design and optimization of the hollow fiber membrane systems including orifices. The present authors documented that the momentum mixing in the spiral wound membranes induced by spacers enhances membrane performance four-five folds with much less degree of energy losses [62]. The presence of porous layer in the hollow fiber membrane modules impedes such improvements by momentum mixing. The penalty of pressure losses caused by the momentum mixing is much larger in hollow fiber

membranes compared to that in spiral wound membranes. Transient and three dimensional effects could have significant influence on the performance of the hollow fiber membrane composites. Three dimensional effects are studied here for a limited operating conditions for only one hollow fiber membrane geometry. The description of the geometry, the method employed and results are presented in the next Chapter.

The sensitivity of the permeability on the membrane performance is investigated by conducting simulations for values of permeance that has order of magnitude variations. P_{CO2} = 2.2 x 10^{-5} is the value of selected for all the results presented above. P_{CO2} = 5.0 x 10^{-6} mol/(m^2.s.Pa) is selected to illustrate how sensitive the membrane performance on the value selected for the permeance of the membrane. The profiles of the Sherwood number along the membrane surface are plotted in Figure 28 for *Re* = 400, *Dp** = 3.7 and *S*/*d* = 10. As it is shown in the figure below the difference in the Sherwood number is 1%, or less. It is clear that the membrane performance is not very sensitive to the selected value of permeance. The value of permeance used in the sensitivity test is in the range of permeance values provided by the manufacturers.

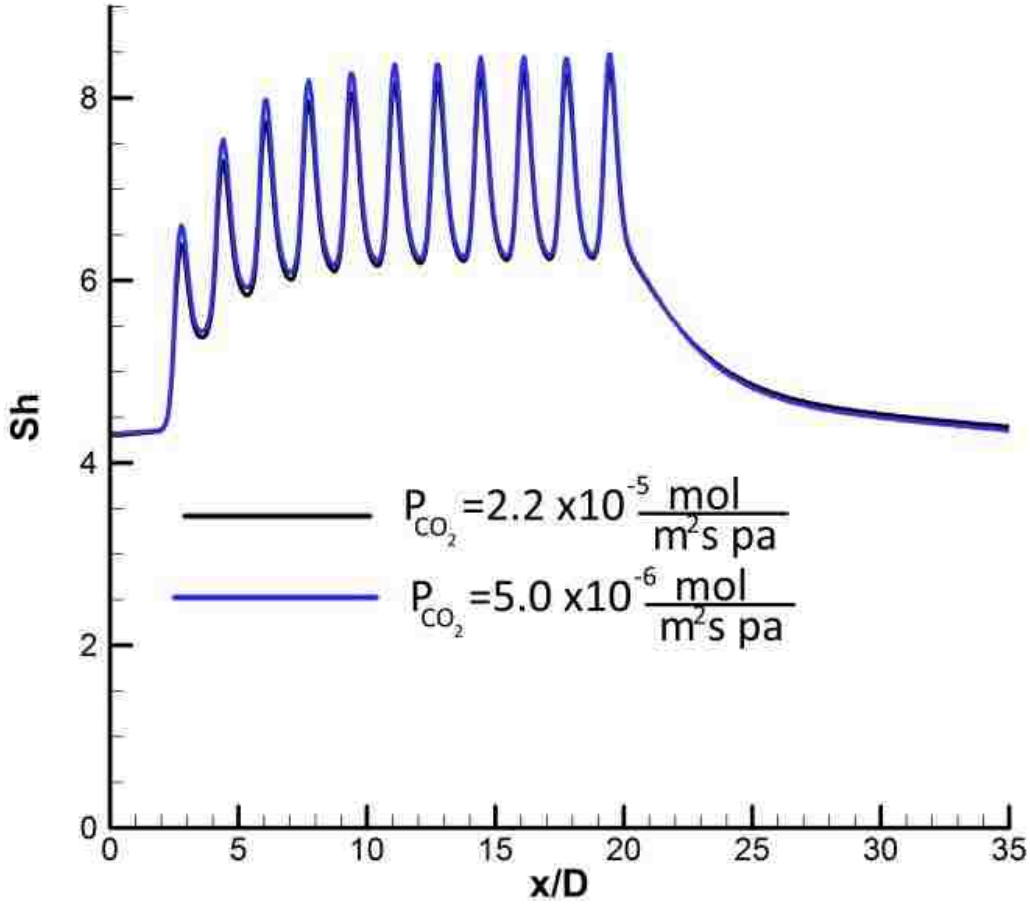

Figure 28: Profiles of the Sherwood number along the membrane for *Re* = 400, *Dp = 3.7 and *S*/*d* = 10. Simulations are conducted for P_{CO2} = 2.2 x 10^{-5} and 5.0 x 10^{-6} mol/(m^2.s.Pa)**

4.2 Hollow fiber membrane module containing diffusers:

4.2.1 Problem description:

Figure 29 describe the schematic of the flow geometry of the hollow fiber membrane module containing diffusers. It consists of an open tubular channel surrounded by a porous layer which is bounded by a dense membrane. The diameter of the open tubular channel is D_1 and the diameter of the module consisting of the porous support layer is D_2, as shown in Figure 29. Uniformly spaced diffusers are placed in an

open channel. The inlet diameter of the diffuser is $d = 0.5\ D_1$ and the spacing between two consecutive diffusers is S. The diffuser exit diameter is the same as the diameter of the open tubular channel, as shown in Figure 29. The binary mixture of CH_4 and CO_2 is treated as an incompressible fluid with uniform physical properties. The flow is axisymmetric and isothermal. The diffusion coefficient is assumed to be independent of the concentration. The permeability of the porous layer is constant. The porous layer is considered to be saturated and the membrane selectivity and permeability are assumed to be constant.

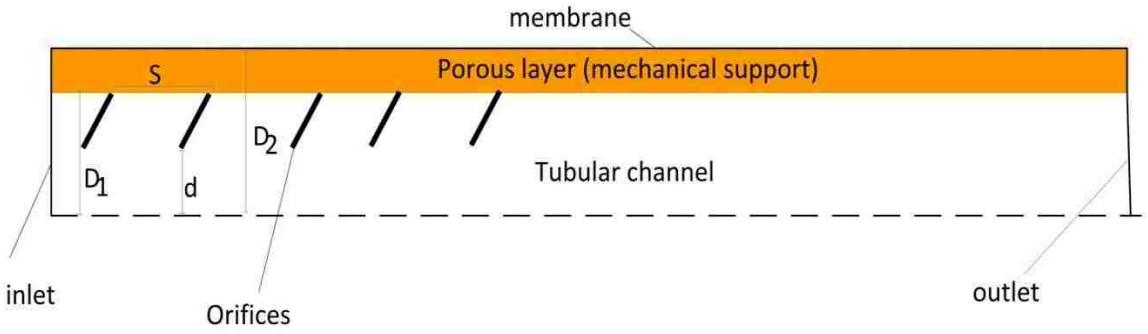

Figure 29: Schematic of the flow geometry and the membrane module of diffusers or conical orifices

4.2.2 Results and Discussions:

Figure 30 displays the steady state stream-wise component of the velocity and the mass fraction of CH_4 contours around first two conical orifices for $Re = 400$ and $S/d = 20$. Figure 30 shows three different values of dimensionless permeability of the porous layer (the Darcy number), Dp^*. The flow is restricted in the open channel and directed into the porous layer by conical orifices, as shown in Figure 30. As porous layer becomes less permeable intensity of the flow through the porous layer decreases while the intensity of the flow near the center of the tubular channel increases. Fluid migrates from the porous

layer to the open channel after passing diffusers since it follows a minimum resistance path. The intensity of the migration from the porous layer to the open layer increases as the permeability of the porous layer decreases. Such flow patterns are repeated after each conical orifice. Figure 30 shows that flow structures induced by diffusers have strong influence on the mass fraction field. The momentum mixing, caused by the conical orifices, not only affects the distribution of the concentration but also influence the mass flux through the membrane. The membrane performance is expected to be improved by the induced momentum mixing.

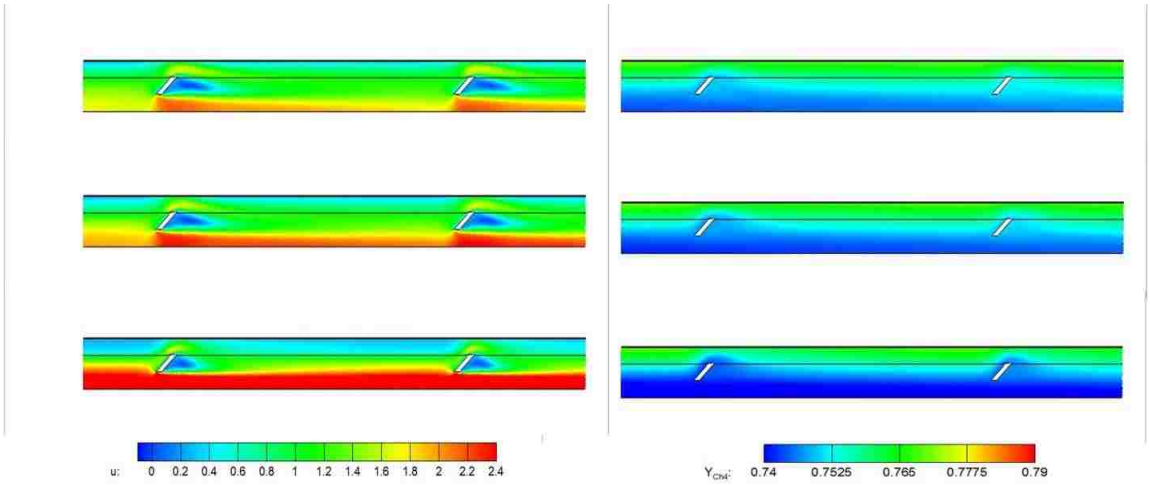

Figure 30: The steady state contours of the stream-wise component of the velocity and the concentration of CH_4 for *Re* = 400 and *S/d* = 10. Images on the left denote the contours of the velocity field and images on the right denote the contours of concentration field. Images from top to bottom are for *Dp=3.7, *Dp**=0.37, and *Dp**=0.037, respectively.**

Figure 31 shows the suction rate along the membrane at *Re* = 100 and 400 for three different values of *Dp**. The suction rate profiles are shown for *S*/*d* = 20 and for a hollow fiber membrane module that is not containing conical orifices. The suction rate along the membrane increases as *Re* is increased in all configurations. There is no

discernible change in the suction rate as the permeability of the support layer is varied in the membrane module without the diffusers, as illustrated in Figure 31. The influence of the conical orifice on the mass flux through the membrane is more pronounced in the membrane module with low permeability support layer, as shown in Figure 31. It is also noticed that the effect of diffusers on the mass flux through the membrane is more profound at higher flow rate.

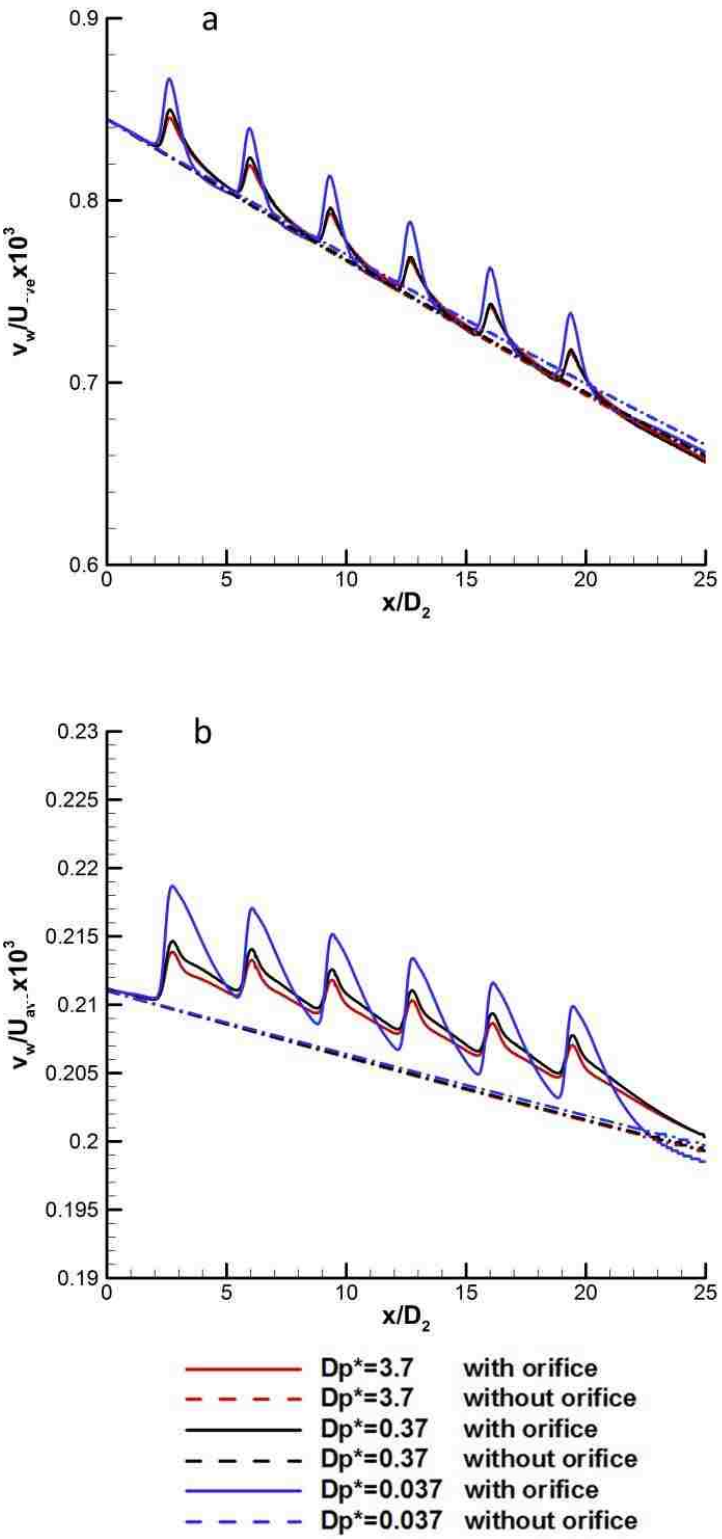

Figure 31: The suction rate along the membrane for (a) *Re* = 400 (b) *Re* =100

Figure 32 shows the local value of the Sherwood number as a function of x at Re = 100 and 400 for S/d = 20. In order to assess the effect of the orifice on the membrane performance the Sherwood number, Sh, is normalized by the Sherwood number of the membrane module without orifices, Sh_0. The value of the normalized Sherwood number, Sh/Sh_0, above unity indicates that the mass flux through the membrane is improved by the placement of the orifice in the feed channel. The Sherwood number fluctuates in the flow direction with a local maxima occurring near the orifices and the local minima occurring near the midpoints between orifices. The value of the local maxima increases and the value of the local minima decreases as the permeability of the porous layer decreases. The effect of the orifice on the hollow fiber membrane performance is strongly dependent on the properties of the support layer, as shown in Figure 32. It is also important to note that the influence of the orifice on the membrane performance is also strongly dependent on the flow rate or Re.

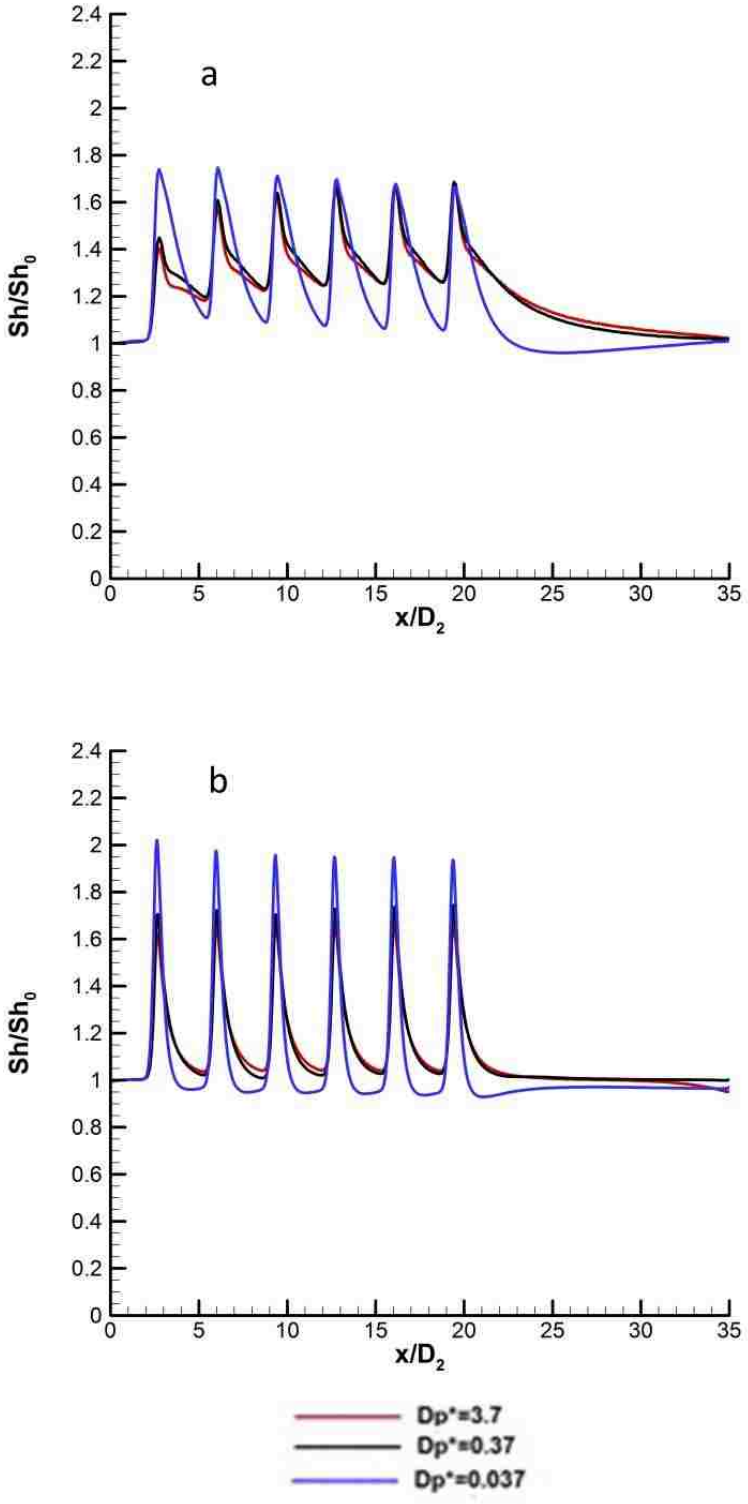

Figure 32: The normalized local value of the Sherwood number vs x/D_2 at (a) Re =400 (b) Re =100

The average value of the Sherwood number is calculated and is plotted in Figure 33 as a function of *Re* for *S*/*d* = 20. The average value of the Sherwood number is determined from the local value from *x/d* of 10 to 25. The Sherwood number is raised by the presence of orifices at all Reynolds number for both geometries with *S*/*d* = 10. The enhancement in the performance of the hollow fiber membrane is greater at higher *Re* in both geometries, as depicted in Figure 33. The degree of the improvement is much less in the module with low permeability support layer, as seen in Figure 33 for *Dp** = 0.037. The effect of the orifice on the membrane performance is very similar for *Dp** of 0.37 and 3.7 in each geometry. The influence of the porous layer is more pronounced at low flow rates. The increase in the average Sherwood number with the presence of orifices is up to 35 % in the geometry.

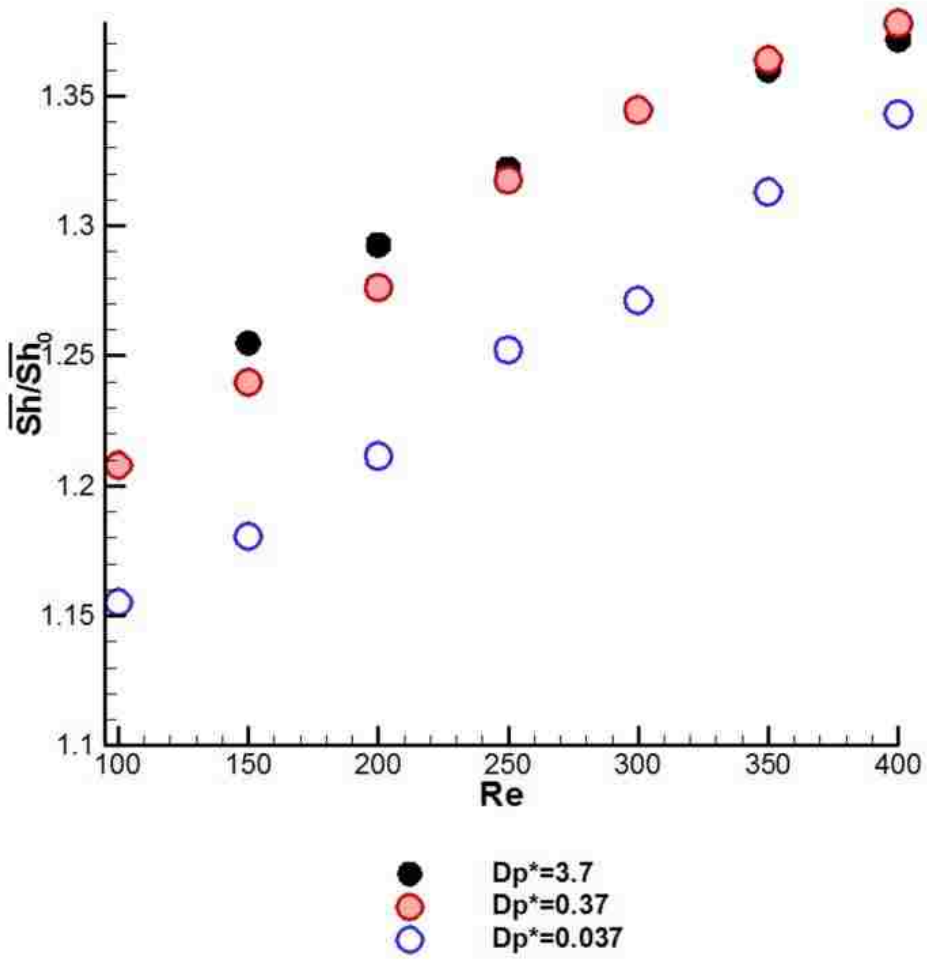

Figure 33: The normalized Sherwood number averaged over the membrane module plotted as a function of the Reynolds number

The friction factor in the hollow fiber membrane with and without orifices is calculated. The average value of the normalized friction factor as a function of *Re* is plotted in Figure 34. The friction factor in the membrane with the orifices is normalized by the friction factor without the orifices. The friction factor increases three-four folds when the orifices are introduced to the hollow fiber membrane in the geometry with *S*/*d* =

20. The increase in the energy losses is higher as flow rate is increased, as shown in Figure 34. The coronial orifice has lower pressure drop compared with vertical orifice.

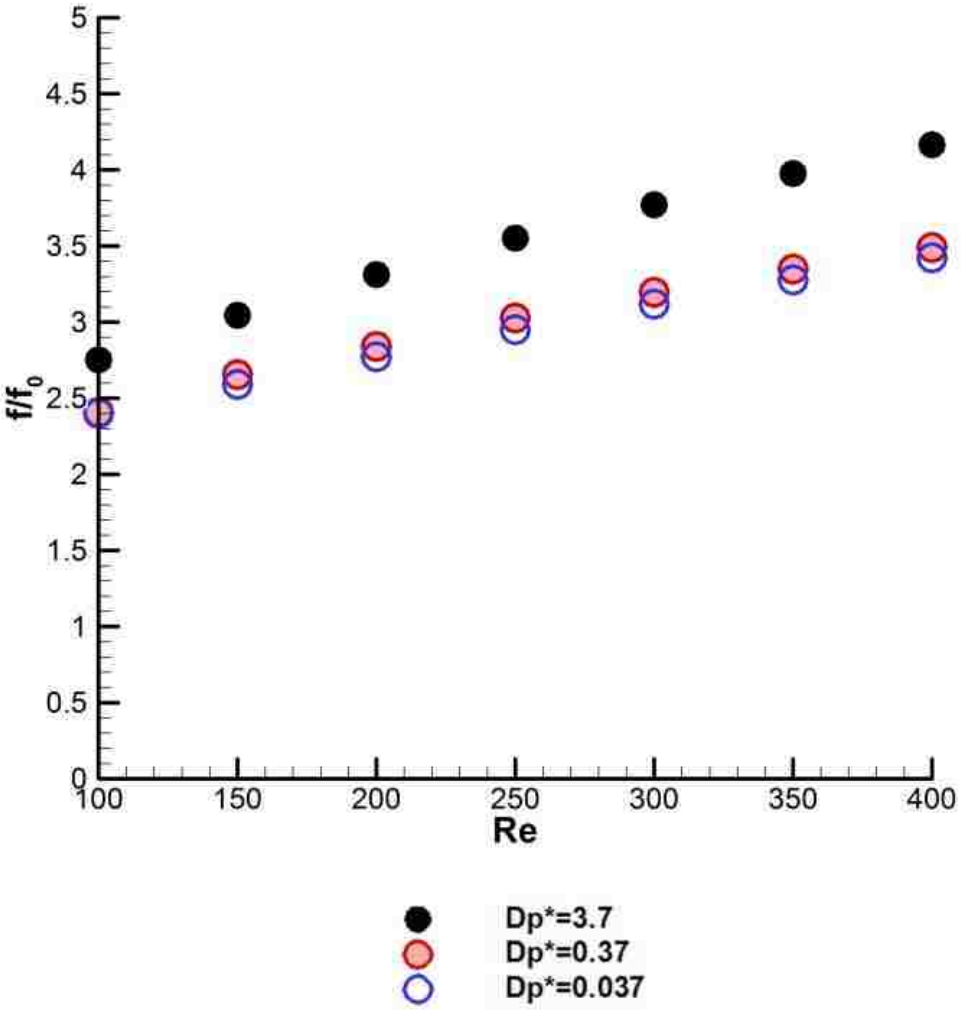

Figure 34: The averaged value of the friction factor as a function of the Reynolds number

The merit number for the efficiency of conical orifices in gas separation process is determined. The merit number based on the membrane enhancement for the same power usage can be written as $(Sh/Sh_0)/(f/f_0)^{1/3}$, as described in Chapter 3. Values of the merit

number are listed in Table 5 at various values of the Reynolds number and the Darcy number for S/d = 20 for a hollow fiber membrane containing uniformly spaced diffusers. Merit number for all cases are slightly below unity; implying that placing orifices in the hollow fiber membrane modules would not be an efficient option. However, this is misleading in the gas-gas separation process considered here. The operation of gas-gas separation studied here requires a high pressure (on the order of several MPa). The pressure of the gas leaving the separation module is very high as well (also on the order of several MPa). The additional pressure drop caused by having conical orifices may not be a factor. The magnitude of the pressure drop in the membrane with orifices is at the level of about 100 Pa per meter at low *Re* and about 1 kPa per meter for high *Re* flows. It should also be mentioned that this study consider only one size of the orifice in one spacing. Further study should be conducted to better understand the efficiency of diffusers with different sizes and different configurations.

		Dp*		
		3.7	0.37	0.037
Re	100	0.86256	0.901272	0.862787
	150	0.865838	0.895382	0.85952
	200	0.867201	0.901211	0.862448
	250	0.866436	0.91091	0.873208
	300	0.863383	0.912904	0.870182
	350	0.858365	0.911681	0.884031
	400	0.852495	0.908436	0.89113

Table 5: Merit numbers of orifice enhancement

4.3 Conclusion

Computational fluid dynamics simulations are conducted to investigate gas-gas separation using a hollow fiber membrane. The CO_2 and CH_4 binary mixture is considered as a fluid flow in the membrane module. The mass flux of each species is determined based on the local partial pressures of each species, the membrane permeability, and the selectivity of the membrane. Steady state simulations are conducted by employing BSL Reynolds Stress turbulence modeling for *Re* up to 400 in geometries with *S*/*d* of 10 and 20 with different shape of offices. The turbulence model is validated for the hollow fiber membrane containing orifices. The hollow fiber membrane performance is enhanced by placing orifices in the feed channel. This study shows that orifices can be used in design of hollow fiber membrane systems for gas separation applications and the spacing and the size of orifices can be important design variables. Further optimization study should be conducted to achieve better membrane enhancement with reasonable level energy losses in hollow fiber membrane systems. Comparing performance of the hollow fiber membrane containing vertical orifices and conical performances for the same spacing of *S*/*d* = 20, the conical orifice has a higher maximum local Sherwood number. This is due to the fact that the mixture passing through the conical orifice impinge on the surface of the membrane. However, the average value of the Sherwood number is similar in both membrane modules. The energy losses in the membrane with conical orifices are lower compared to those in the membrane with vertical orifices at the same flow rates.

Chapter 5: 3D Hollow Fiber Membrane with grove

5.1 Problem description:

The schematic of the three-dimensional flow geometry is illustrated in Figure 35. It consists of an open tubular channel surrounded by a porous layer that is bounded by a dense membrane. The diameter of the open tubular channel is D_1 and the diameter of the module consisting of the porous support layer is D_2, as shown in Figure 35. At the interface between the empty tubular pipe and the porous layer helical grooves are placed with a uniform pitch. The width of the groove is $w = 0.05\ D_1$ and the pitch size is $S = 2.1\ D_1$. The binary mixture of CH_4 and CO_2 is treated as an incompressible fluid with uniform physical properties. The flow is isothermal. The diffusion coefficient is assumed to be independent of the concentration. The permeability of the porous layer is constant. The porous layer is considered to be saturated and the membrane selectivity and permeability are assumed to be constant.

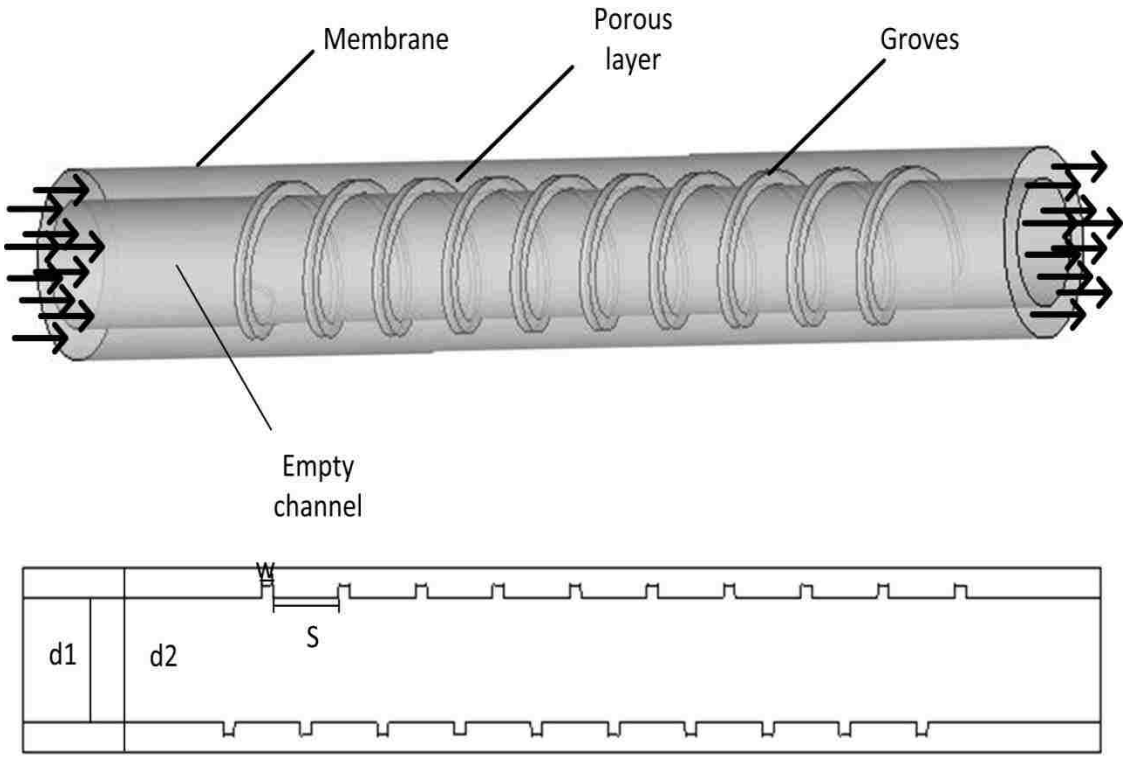

Figure 35: Schematic of the three dimensional flow geometry and the hollow fiber membrane module containing grooves

5.2 Results and Discussions

Figure 36 depicts the steady state contours of the stream-wise, radial, and tangential components of the velocity and the concentration of CH_4 in the *r*-*x* plane with an angle of $\pi/2$. The grooves restrict flows in the hollow fiber membrane and direct fluid to the empty channel, as shown in Figure 36a. The grooves enhance the rotational velocity in the region near interface. However, the local rotational velocity created by grooves does not help mixing in feed channel. Such flow patterns are repeated after each passed grooves. These flow structures induced by grooves have strong influence on the concentration field, as illustrated in Figure 36d. The momentum mixing, caused by the grooves, only affects the distribution of the concentration in the region near the interface.

However the grooves help to build more pronounced concentration boundary layer near the membrane. This would results in the decrease of the membrane performance.

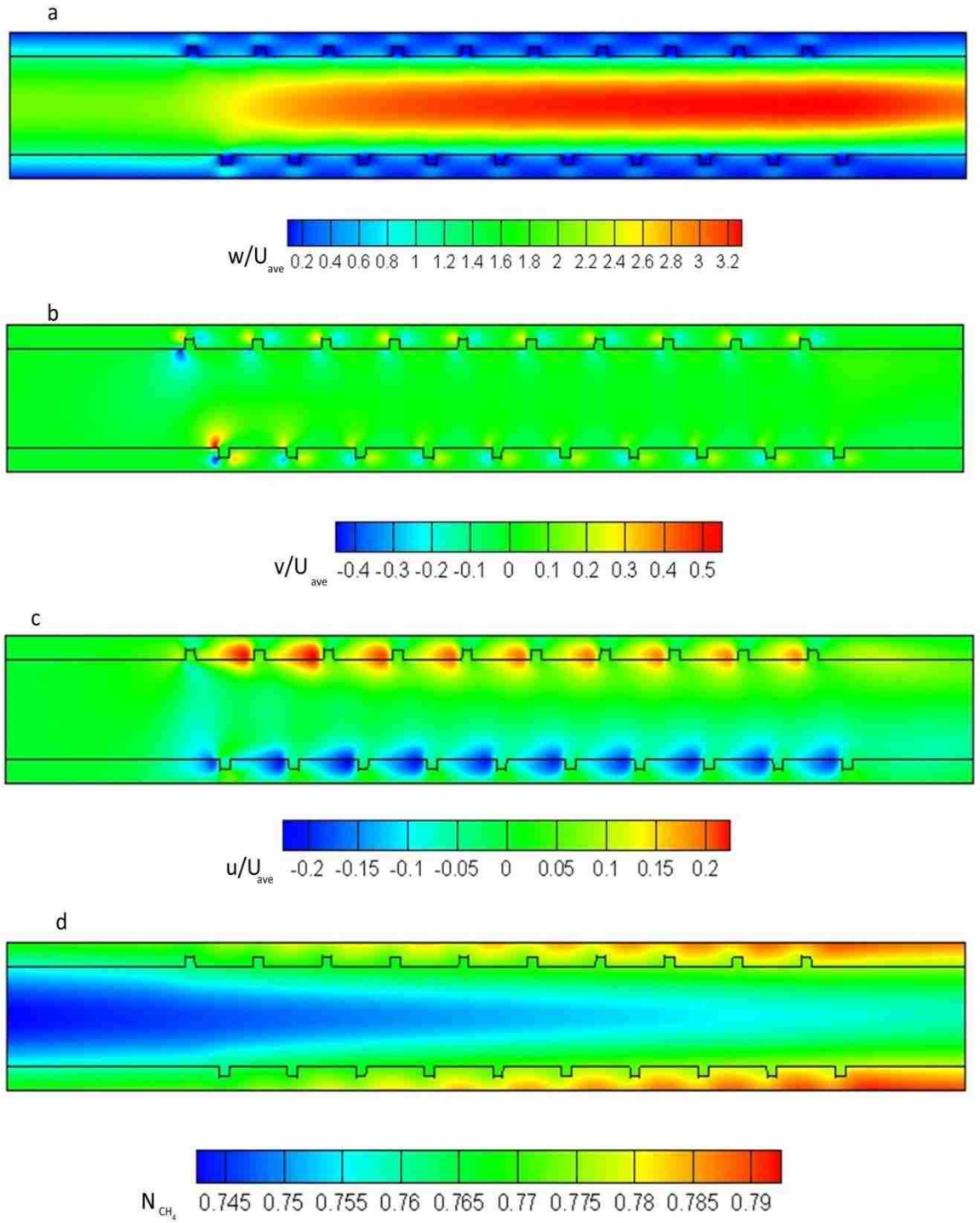

Figure 36: The steady state contours of the velocity and the concentration of CH_4

Figure 37 shows the suction rate along the membrane at *Re* = 100 and *Dp**=3.7 for both with and without helical grooves. The grooved has an adverse effect on the suction rate. Because the helical grooves direct the flow into the center of empty channel and help to create the concentration boundary layer attached to the surface of membrane.

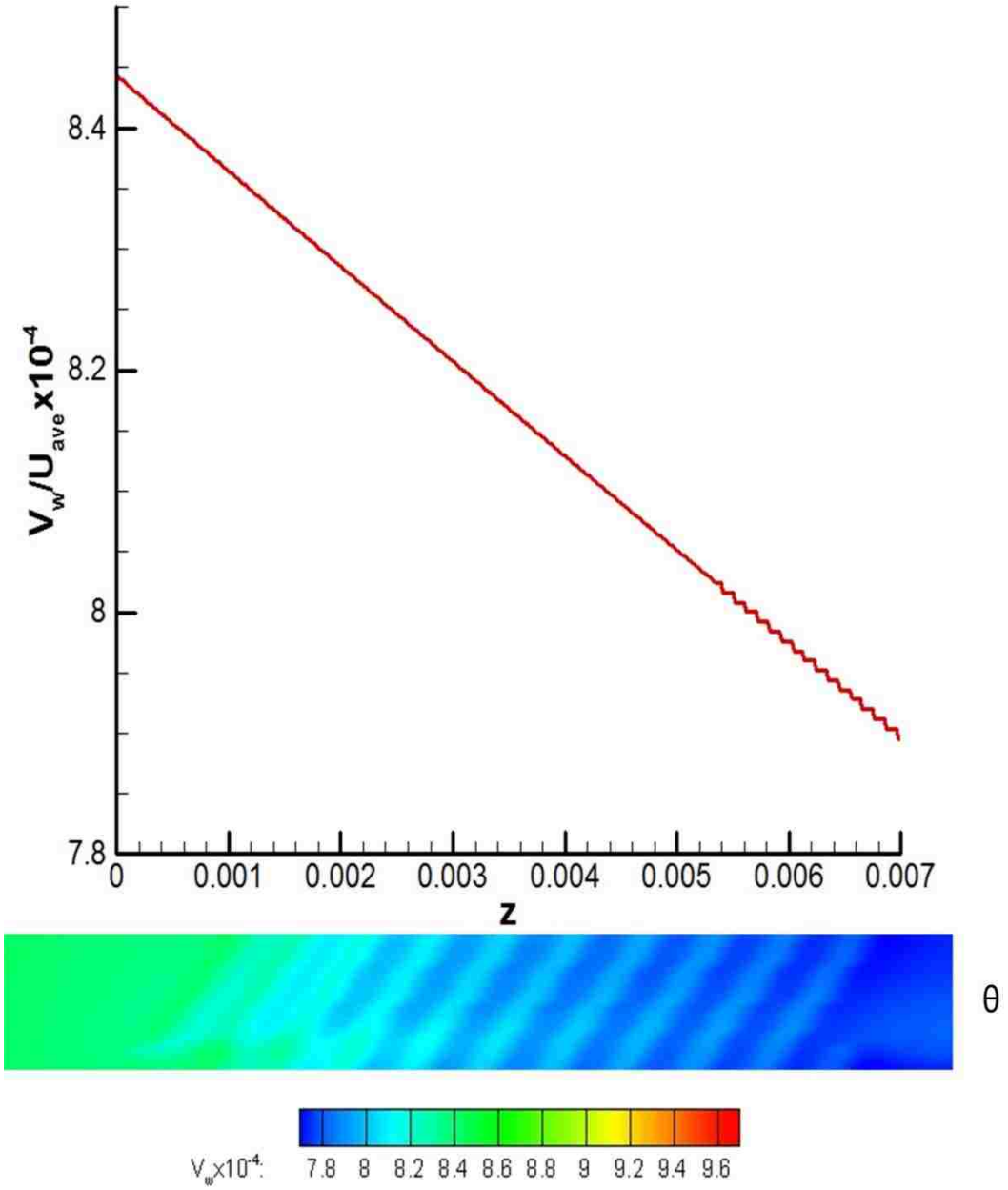

Figure 37: The suction rate along the membrane in a hollow fiber membrane (a) without grooves, (b) with helical grooves

Figure 38 shows the local value of the Sherwood number as a function of *x* at *Re* = 100 for Dp*=3.7. In order to assess the effect of the grooves on the membrane performance the Sherwood number, *Sh*, is normalized by the Sherwood number of the

membrane module without orifices, Sh_0. The value of the normalized Sherwood number, Sh/Sh_0, above unity in early stage of the groove indicates that the mass flux through the membrane is improved by the placement of the groove in the feed channel. However, normalized Sherwood number below the unity because the grooves direct flow to the center of empty channel and help to create the concentration boundary layer. The Sherwood number fluctuates in the flow direction with a local maxima occurring near the groove and the local minima occurring near the midpoints between helical grooves. The effect of the helical on the hollow fiber membrane performance is unfavorable, as shown in Figure 38. This result proves that careful selection of the grooves is necessary in the optimization process of the hollow fiber membrane design.

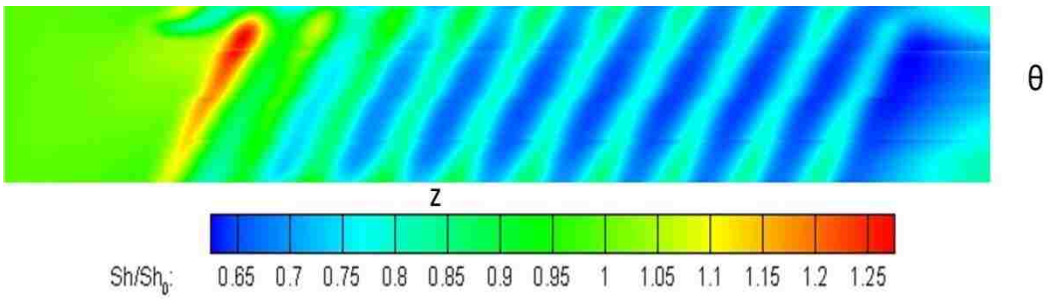

Figure 38: The normalized local value of the Sherwood number

5.3 Conclusion

Computational fluid dynamics simulations are conducted to investigate gas-gas separation using a hollow fiber membrane. The CO_2 and CH_4 binary mixture is considered as a fluid flow in the membrane module. The mass flux of each species is determined based on the local partial pressures of each species, the membrane permeability, and the selectivity of the membrane. Steady state simulations are conducted

by employing BSL Reynolds Stress turbulence modeling for *Re* 100 in geometry with helical groove. The hollow fiber membrane performance is decreased by placing grooves in the feed channel. This study shows that groove is unfavorable to be selected in design of hollow fiber membrane systems for gas separation applications. It has to be stated here only one dimension and configuration of grooves is studied here. Comprehensive optimization and design of these grooves can still produce desirable effects on the membrane performance in hollow fiber membrane modules considered here.

Chapter 6: Summary

Computational fluid dynamics simulations are conducted to study gas separation process using spiral wound and hollow fiber membrane modules. The effect of momentum mixing on the membrane performances is investigated by introducing flow restricting devices into the feed channel. There have been extensive investigations to study the effect of momentum mixing on the membrane performances for water treatment processes using reverse osmosis. However, the effect of mixing on the membrane performance in gas-gas separation process using membranes has not been studied. The concentration of the salt in saline water ($mole_{salt}/mole_{water}$) varies from 0.002 to 0.04. Since the mole fraction of the salt in water-salt mixture is small the effect of salt flux in the momentum conservation is neglected when it is compared with the effect of the water flux. For the mass transport through the membrane, the salt flux is typically assumed to be linearly proportional to the water flux. However, neither assumption can be used in the gas-gas separation where the concentrations of both species are comparable. In a flux model for gas-gas separation, the effect of the molar flux of both species has to be considered in the momentum and mass transports through the membrane. In the present study, the model proposed by the present author considers these effects. This makes the model presented unique in both its ability to accurately model gas-gas separation flows and in its adaptability to other membrane flow applications. There exists no previous model which could study these unsteady membrane flows without making some of the aforementioned assumptions to determine the mass fluxes of species through the membrane.

Steady and transient two dimensional flows are characterized in a spiral wound membrane module that contains different shape and size of spacers for a wide range of Reynolds number. Flow characteristics are also determined in a hollow fiber membrane that contains flow restricting devices such as orifices, conical orifices (diffusers) and grooves. Two and three dimensional flows in hollow fiber membrane modules are characterized for a wide range of Reynold number and the Darcy number. Detailed descriptions of the geometry of both units are presented along with the detailed mathematical models that govern the velocity and concentration fields. The unique flux model introduced first by the present author is presented and described. The membrane flux model applied to gas-gas separation and possibly for other separation processes is derived from the first principal. The detailed derivation of the membrane flux model is given in this document. This unique model treats membrane as a functional surface. The mass flux of each species is determined based on the local partial pressures of each species, the permeability, and the selectivity of the membrane.

The binary mixture of CO_2 and CH_4 is considered in the separation process using membranes. Both steady and transient simulations are conducted by employing k-ω and LES turbulence modeling for *Re* up to 1000 to study membrane performance in a spiral wound membrane. The effect of the shape, spacing and the configuration of spacers on membrane performance is studied. The amount of CO_2 extracted increases and the amount CH_4 lost decreases when spacers are placed inside the feed channel. Such performance enhancement is more pronounced at higher flow rates. Staggering the spacers, increasing the frequency of the spacers, and introducing triangular shaped spacers increase the mass transport through the membrane. Not only the mass transport

through the membrane is increased by placing turbulators, it actually increases the passage of CO_2 while it decreases to loss of CH_4. The pressure drop increases by the presence of the spacers, but such increase in the pressure drop is very small compared to the operating pressure of the membrane. Hence, its effect on the membrane performance is not significant. This study shows that spacers should be an important part of membrane systems used in gas-gas separation.

The separation of CO_2 from CH_4 is considered in the separation process using a hollow fiber membrane that contains flow restricting devices. Two dimensional flows in the membrane module are investigated for different arrangements of orifices and diffusers. The mass fluxes of CO_2 and CH_4 are determined based on the local partial pressures of each species, the membrane permeability, and the selectivity of the membrane. Steady state simulations are conducted by employing BSL Reynolds Stress turbulence modeling for *Re* up to 400 in geometries with *S*/*d* of 10 and 20. The turbulence model is validated by comparing predicted results with measurements reported by previous investigators. The hollow fiber membrane performance is enhanced by placing orifices or diffusers in the feed channel. This study shows that orifices or diffusers can be used in design of hollow fiber membrane systems for gas separation applications and the spacing and the size of orifices or diffusers can be important design variables. It is also shown here that the porous support layer decreases the performance of the hollow fiber membrane. Orifices or diffusers are introduced to alleviate the adverse effects of the porous layer on the membrane performance. Further optimization study should be conducted to achieve better membrane enhancement with reasonable level energy losses in hollow fiber membrane systems.

Three dimensional flows are studied in a hollow fiber module containing helical grooves. The binary mixture of CO_2 and CH_4 is considered in the membrane hollow fiber module with helical grooves. The mass flux of each species is determined based on the local partial pressures of each species, the membrane permeability, and the selectivity of the membrane. Steady state simulations are conducted by employing BSL Reynolds Stress turbulence modeling for *Re* 100 in the hollow fiber membrane geometry with helical grooves. Based on the study of one configuration and one geometry of helical grooves at *Re* = 100 it is concluded that the hollow fiber membrane performance is decreased by placing grooves in the feed channel. It may be undesirable to insert grooves into the porous support layer for gas separation applications using hollow fiber membrane modules.

This work can be extended to three dimensional effects on the spiral wound membrane, helical fin in hollow fiber membrane, flow over banks of hollow fiber membrane, and experimental investigation. Spacers in spiral wound membrane are connected with inclined angle with direction of flow. The inclined angle effects on flow structure and momentum mixing. The helical fin in hollow fiber can improve the membrane performance. In the some gas-gas separation application, the feed mixture flow outside of hollow fiber membrane and permeate flow inside hollow fiber membrane. there is lack experimental investigation studied the effect of momentum mixing effect on the membrane performance.

REFERENCES

[1] M.G. Süer, N. Baç, L. Yilmaz, Gas permeation characteristics of polymer-zeolite mixed matrix membranes, Journal of Membrane Science, 91(1–2) (1994) 77-86.
[2] C.M. Zimmerman, A. Singh, W.J. Koros, Tailoring mixed matrix composite membranes for gas separations, Journal of Membrane Science, 137(1–2) (1997) 145-154.
[3] A.F. Ismail, L.I.B. David, A review on the latest development of carbon membranes for gas separation, Journal of Membrane Science, 193(1) (2001) 1-18.
[4] J.E. Bara, E.S. Hatakeyama, D.L. Gin, R.D. Noble, Improving CO2 permeability in polymerized room-temperature ionic liquid gas separation membranes through the formation of a solid composite with a room-temperature ionic liquid, Polymers for Advanced Technologies, 19(10) (2008) 1415-1420.
[5] M. Palomino, A. Corma, J.L. Jorda, F. Rey, S. Valencia, Zeolite Rho: a highly selective adsorbent for CO2/CH4 separation induced by a structural phase modification, Chemical Communications, 48(2) (2012) 215-217.
[6] G.J. Francisco, A. Chakma, X. Feng, Separation of carbon dioxide from nitrogen using diethanolamine-impregnated poly(vinyl alcohol) membranes, Separation and Purification Technology, 71(2) (2010) 205-213.
[7] D.D. Iarikov, P. Hacarlioglu, S.T. Oyama, Supported room temperature ionic liquid membranes for CO2/CH4 separation, Chemical Engineering Journal, 166(1) (2011) 401-406.
[8] S.A.M. Marzouk, M.H. Al-Marzouqi, M.H. El-Naas, N. Abdullatif, Z.M. Ismail, Removal of carbon dioxide from pressurized CO2–CH4 gas mixture using hollow fiber membrane contactors, Journal of Membrane Science, 351(1–2) (2010) 21-27.
[9] R. Pathare, R. Agrawal, Design of membrane cascades for gas separation, Journal of Membrane Science, 364(1–2) (2010) 263-277.
[10] R. Qi, M.A. Henson, Optimal design of spiral-wound membrane networks for gas separations, Journal of Membrane Science, 148(1) (1998) 71-89.
[11] R.E. Babcock, R.W. Spillman, C.S. Goddin, T.E. Cooley, Natural gas cleanup: A comparison of membrane and amine treatment processes, Energy progress, 8(3) (1988) 135-142.
[12] S.K. Karode, A. Kumar, Flow visualization through spacer filled channels by computational fluid dynamics I.: Pressure drop and shear rate calculations for flat sheet geometry, Journal of Membrane Science, 193(1) (2001) 69-84.
[13] A. Saeed, R. Vuthaluru, Y. Yang, H.B. Vuthaluru, Effect of feed spacer arrangement on flow dynamics through spacer filled membranes, Desalination, 285(0) (2012) 163-169.
[14] G.A. Fimbres-Weihs, D.E. Wiley, D.F. Fletcher, Unsteady Flows with Mass Transfer in Narrow Zigzag Spacer-Filled Channels: A Numerical Study, Industrial & Engineering Chemistry Research, 45(19) (2006) 6594-6603.
[15] V.V. Ranade, A. Kumar, Fluid dynamics of spacer filled rectangular and curvilinear channels, Journal of Membrane Science, 271(1–2) (2006) 1-15.
[16] J. Schwinge, D.E. Wiley, D.F. Fletcher, A CFD study of unsteady flow in narrow spacer-filled channels for spiral-wound membrane modules, Desalination, 146(1–3) (2002) 195-201.

[17] V.V. Ranade, A. Kumar, Comparison of flow structures in spacer-filled flat and annular channels, Desalination, 191(1–3) (2006) 236-244.
[18] S. Al-Sharif, M. Albeirutty, A. Cipollina, G. Micale, Modelling flow and heat transfer in spacer-filled membrane distillation channels using open source CFD code, Desalination, 311(0) (2013) 103-112.
[19] M. Shakaib, S.M.F. Hasani, M. Mahmood, CFD modeling for flow and mass transfer in spacer-obstructed membrane feed channels, Journal of Membrane Science, 326(2) (2009) 270-284.
[20] S. Pal, R. Bharihoke, S. Chakraborty, S.K. Ghatak, S. De, S. DasGupta, An experimental and theoretical analysis of turbulence promoter assisted ultrafiltration of synthetic fruit juice, Separation and Purification Technology, 62(3) (2008) 659-667.
[21] A. Subramani, S. Kim, E.M.V. Hoek, Pressure, flow, and concentration profiles in open and spacer-filled membrane channels, Journal of Membrane Science, 277(1–2) (2006) 7-17.
[22] G. Guillen, E.M.V. Hoek, Modeling the impacts of feed spacer geometry on reverse osmosis and nanofiltration processes, Chemical Engineering Journal, 149(1–3) (2009) 221-231.
[23] E. Lyster, Y. Cohen, Numerical study of concentration polarization in a rectangular reverse osmosis membrane channel: Permeate flux variation and hydrodynamic end effects, Journal of Membrane Science, 303(1–2) (2007) 140-153.
[24] J.P.G. Villaluenga, Y. Cohen, Numerical model of non-isothermal pervaporation in a rectangular channel, Journal of Membrane Science, 260(1–2) (2005) 119-130.
[25] D.F. Fletcher, D.E. Wiley, A computational fluids dynamics study of buoyancy effects in reverse osmosis, Journal of Membrane Science, 245(1–2) (2004) 175-181.
[26] G.A. Fimbres-Weihs, D.E. Wiley, Numerical study of mass transfer in three-dimensional spacer-filled narrow channels with steady flow, Journal of Membrane Science, 306(1–2) (2007) 228-243.
[27] A.L. Ahmad, K.K. Lau, Impact of different spacer filaments geometries on 2D unsteady hydrodynamics and concentration polarization in spiral wound membrane channel, Journal of Membrane Science, 286(1–2) (2006) 77-92.
[28] K.K. Lau, M.Z. Abu Bakar, A.L. Ahmad, T. Murugesan, Feed spacer mesh angle: 3D modeling, simulation and optimization based on unsteady hydrodynamic in spiral wound membrane channel, Journal of Membrane Science, 343(1–2) (2009) 16-33.
[29] S. Ma, L. Song, Numerical study on permeate flux enhancement by spacers in a crossflow reverse osmosis channel, Journal of Membrane Science, 284(1–2) (2006) 102-109.
[30] S. Ma, L. Song, S.L. Ong, W.J. Ng, A 2-D streamline upwind Petrov/Galerkin finite element model for concentration polarization in spiral wound reverse osmosis modules, Journal of Membrane Science, 244(1–2) (2004) 129-139.
[31] A.E. Anqi, N. Alkhamis, A. Oztekin, Numerical simulation of brackish water desalination by a reverse osmosis membrane, Desalination, 369(0) (2015) 156-164.
[32] P.K. Kundu, A. Chakma, X. Feng, Modelling of multicomponent gas separation with asymmetric hollow fibre membranes—methane enrichment from biogas, The Canadian Journal of Chemical Engineering, 91(6) (2013) 1092-1102.

[33] P.K. Kundu, A. Chakma, X. Feng, Simulation of binary gas separation with asymmetric hollow fibre membranes and case studies of air separation, The Canadian Journal of Chemical Engineering, 90(5) (2012) 1253-1268.
[34] T. Sugiyama, N. Miyahara, M. Tanaka, K. Munakata, I. Yamamoto, A simulation model for transient response of a gas separation module using a hollow fiber membrane, Fusion Engineering and Design, 86(9) (2011) 2743-2746.
[35] H.-Y. Zhang, R. Wang, D.T. Liang, J.H. Tay, Modeling and experimental study of CO< sub> 2</sub> absorption in a hollow fiber membrane contactor, Journal of Membrane Science, 279(1) (2006) 301-310.
[36] B. Chen, Z. Gao, W. Jin, S. Zheng, Analytical mass transfer solution of longitudinal laminar flow of Happel's free surface model, International Journal of Heat and Mass Transfer, 54(17) (2011) 4000-4008.
[37] P. Keshavarz, J. Fathikalajahi, S. Ayatollahi, Mathematical modeling of the simultaneous absorption of carbon dioxide and hydrogen sulfide in a hollow fiber membrane contactor, Separation and Purification Technology, 63(1) (2008) 145-155.
[38] A. Portugal, F. Magalhães, A. Mendes, Carbon dioxide removal from anaesthetic gas circuits using hollow fiber membrane contactors with amino acid salt solutions, Journal of Membrane Science, 339(1) (2009) 275-286.
[39] R. Wang, H. Zhang, P. Feron, D. Liang, Influence of membrane wetting on CO< sub> 2</sub> capture in microporous hollow fiber membrane contactors, Separation and Purification Technology, 46(1) (2005) 33-40.
[40] F. Vinther, M. Pinelo, M. Brøns, G. Jonsson, A.S. Meyer, Mathematical modelling of dextran filtration through hollow fibre membranes, Separation and Purification Technology, 125(0) (2014) 21-36.
[41] G.S. Beavers, E.M. Sparrow, R.A. Magnuson, Experiments on Coupled Parallel Flows in a Channel and a Bounding Porous Medium, Journal of Fluids Engineering, 92(4) (1970) 6.
[42] S.K. Karode, Laminar flow in channels with porous walls, revisited, Journal of Membrane Science, 191(1–2) (2001) 237-241.
[43] R. Ghidossi, J. Daurelle, D. Veyret, P. Moulin, Simplified CFD approach of a hollow fiber ultrafiltration system, Chemical Engineering Journal, 123(3) (2006) 117-125.
[44] N.S. Hanspal, A. Waghode, V. Nassehi, R.J. Wakeman, Development of a predictive mathematical model for coupled stokes/Darcy flows in cross-flow membrane filtration, Chemical Engineering Journal, 149(1) (2009) 132-142.
[45] V. Nassehi, Modelling of combined Navier–Stokes and Darcy flows in crossflow membrane filtration, Chemical Engineering Science, 53(6) (1998) 1253-1265.
[46] B. Marcos, C. Moresoli, J. Skorepova, B. Vaughan, CFD modeling of a transient hollow fiber ultrafiltration system for protein concentration, Journal of Membrane Science, 337(1–2) (2009) 136-144.
[47] F.R. Menter, Improved two-equation k-turbulence models for aerodynamic flows, NASA Technical Memorandum, 103975(1_) (1992) 3t.
[48] J. Smagorinsky, GENERAL CIRCULATION EXPERIMENTS WITH THE PRIMITIVE EQUATIONS, Monthly Weather Review, 91(3) (1963) 99-164.
[49] J.W. Deardorff, A numerical study of three-dimensional turbulent channel flow at large Reynolds numbers, Journal of Fluid Mechanics, 41(02) (1970) 453-480.

[50] P. Sagaut, Large eddy simulation for incompressible flows, Springer, 2002.
[51] S.B. Pope, Turbulent flows, Cambridge university press, 2000.
[52] A. Leonard, Energy Cascade in Large-Eddy Simulations of Turbulent Fluid Flows, in: F.N. Frenkiel, R.E. Munn (Eds.) Advances in Geophysics, Elsevier, 1975, pp. 237-248.
[53] D.A. Nield, A. Bejan, Convection in porous media, Springer Science & Business Media, 2006.
[54] E. Ucar, M. Mobedi, I. Pop, Effect of an inserted porous layer located at a wall of a parallel plate channel on forced convection heat transfer, Transport in porous media, 98(1) (2013) 35-57.
[55] G.S. Beavers, D.D. Joseph, Boundary conditions at a naturally permeable wall, Journal of fluid mechanics, 30(01) (1967) 197-207.
[56] N. Alkhamis, A. Anqi, D.E. Oztekin, A. Alsaiari, A. Oztekin, Enhancing gas separation across a membrane with pulsating flow, in: 10th International Conference on Heat Transfer, Fluid Mechanics and Thermodynamics, American Society of Mechanical Engineers, 2014.
[57] N. Alkhamis, D.E. Oztekin, A.E. Anqi, A. Alsaiari, A. Oztekin, Numerical study of gas separation using a membrane, International Journal of Heat and Mass Transfer, 80 (2015) 835-843.
[58] Nawaf Alkhamis, A.E.A. Dennis E Oztekin, Abdulmohsen Alsaiari, Alparslan Oztekin, Enhancing gas sepration across a membrane with pulsating flow, in: International Conference on Heat Transfer, Fluid Mechanics and Thermodynamics, International Conference on Heat Transfer, Fluid Mechanics and Thermodynamics, Orlando, FL, 2014.
[59] N. Alkhamis, A. Anqi, D.E. Oztekin, A. Alsaiari, A. Oztekin, Gas Separation Using a Membrane, in: ASME 2013 International Mechanical Engineering Congress and Exposition, American Society of Mechanical Engineers, 2013, pp. V07AT08A039-V007AT008A039.
[60] R. Davis, E. Moore, L. Purtell, A numerical-experimental study of confined flow around rectangular cylinders, Physics of Fluids (1958-1988), 27(1) (1984) 46-59.
[61] A. Roshko, Experiments on the flow past a circular cylinder at very high Reynolds number, J. Fluid Mech, 10(3) (1961) 345-356.
[62] N. Alkhamis, A. Anqi, D.E. Oztekin, A. Alsaiari, A. Oztekin, Gas separation using a membrane, in: ASME 2014 International Mechanical Engineering Congress and Exposition, American Society of Mechanical Engineers, 2014, pp. IMECE2014-37299.
[63] N. Alkhamis, A.E. Anqi, A. Oztekin, Computational Study of Gas Separation Using a Hollow Fiber Membrane, Inernational Journal of Heat and Mass Transfer, accepted (2015).
[64] F. Johansen, Flow through pipe orifices at low Reynolds numbers, Proceedings of the Royal Society of London. Series A, 126(801) (1930) 231-245.

VITA

Name Nawaf Yahya Alkhamis

Address Mechanical Engineering Department
College of Engineering
King Abdulaziz University
Jeddah 21589
Saudi Arabia

Email nalkhamis@kau.edu.sa

Education *Lehigh University*
P.C. Rossin College of Engineering and Applied Science, Bethlehem, PA
Doctor of Philosophy (2012 – 2015) Major: Mechanical Engineering
Research Area: Computational Study of Gas Separation by Using Membrane

- Utilized numerical approaches such as computational fluid dynamics (CFD) to predicted mass transfer Coefficient and flow field for Spiral Wound membrane with different configuration of spacer and Hollow fiber membrane with turbulator. As results of this work, higher performance and economical solution for gas separation processes

Texas A&M University
Dwight Look College of Engineering, College Station, TX
Master of Science (2007 – 2009) Major: Mechanical Engineering
Research Area: Gas Turbine Cooling Blades

- Conducted experimental work to measure heat transfer coefficient and pressure drop for channel with different configuration of ribs at High Reynolds number. This lead to enhance the land based gas turbine performance

King Abdulaziz University
College of Engineering, Jeddah, Saudi Arabia
Bachelor of Science (1999-2004) Major: Thermal Engineering
Senior Project: Tested heat transfer coefficient for single pulsating impinging jet